Computer Programs for Tsunami Propagation and Inundation

Philip L.-F. Liu *, Seung-Buhm Woo * and Yong-Sik Cho **

* School of Civil and Environmental Engineering
Cornell University, Ithaca, NY 14853, USA

** Department of Civil Engineering and the Institute of
Waterway Industry, Sejong University, Seoul 143-747, Korea

October, 1998

Abstract

In this report, a nested multi-grid finite difference model for simulating tsunami propagation and runup is presented. The model has the option to use either the linear or the nonlinear version of shallow-water equations with different type of coordinate system (i.e. either Cartesian or Spherical) in each subregion. Although different grid sizes are employed in each subregion, physical variables in all subregions are solved simultaneously. The model also allows any ratio of grid sizes between two adjacent subregions.

A Fortran computer program for the model is documented in this report. Detailed descriptions for the main programs and subroutines are provided. A manual that describes input and output data files is also given with examples. This model could easily be applied to different cases by changing input and control files only.

In the linear component of the model, the linear shallow-water equations are discretized with the explicit leap-frog finite difference scheme. For the constant depth case the numerical dispersion induced by the leap-frog scheme is optimally controlled by choosing appropriate time step size and grid sizes so that it plays an equivalent role of the frequency dispersion represented in the linear Boussinesq equations.

In the nonlinear component of the model, nonlinear shallow-water equations are also discretized with the explicit leap-frog finite difference scheme, whereas nonlinear convective terms are discretized with an upwind scheme. A moving boundary treatment is applied to track movements of the shoreline.

To verify the nested multi-grid model, several numerical examples are presented and some of them are compared with available analytical solutions. In general, good agreement is observed.

The multi-grid coupled model is used to simulate the 1986 Hwa-lien (Taiwan) tsunami occurred in 1986. The general feature of the refraction and diffraction of

tsunami around Taiwan is presented. The numerical results are compared with the tide-gauge data at Hwa-lien harbor, Ishigaki harbor (Ishigaki island, Japan) and Hirara harbor (Miyako-jima island, Japan). A general agreement is obtained in terms of the dominant period of oscillations in the Hwa-lien harbor and the arrival time of the first leading wave at Ishigaki island and Hirara harbor. A maximum inundation map at Hwa-lien harbor is produced.

Acknowledgment

Contents

1 Introduction

Tsunami is a Japanese word that is the combination of two word roots : "tsu" means harbor and "nami" means wave. Therefore, tsunami literally means "harbor wave." The word was originally created to describe large amplitude oscillations in a harbor under the resonance condition. Most of major tsunamis have been generated by undersea earthquakes. The impulsive sea floor movement in the earthquake source (fault) region causes the deformation of water surface instantaneously. The suddenly gained potential energy is converted to kinetic energy by the gravitational force, which serves as the restoring force of the system.

The leading wave of a tsunami has a wavelength proportional to the longitudinal dimension of the earthquake source region, which could be of the order of magnitude of several hundreds or a thousand kilometers for a major earthquake. Therefore, the leading tsunami can be considered as a long wave with a propagating speed that is proportional to $(gh)^{1/2}$, where h is the water depth. For example, in the Pacific ocean where the average depth is about 4 km, the leading wave of a tsunami travels approximately at a speed of 700 km/hr. Although the wave speed is high, the amplitude of a typical tsunami in the deep ocean, approximately 1 or 2 m, is usually very small in comparison with the wavelength. The corresponding orbital velocity and the associated momentum fluxes are also small in the deep ocean. However, as a tsunami reaches a coastal region where the water depth becomes shallow, the amplitude of the tsunami increases and the wavelength decreases. A tsunami could cause severe coastal flooding and property damages.

Tsunamis have been observed and recorded since ancient times, especially in Japan and the Mediterranean areas. The earliest recorded tsunami occurred in 2,000 B.C. off the coast of Syria (Lander and Lockridge, 1989). The oldest reference of tsunami record is dated back to the 16th century in the United States (Cox, 1987).

1

During this century, more than 100 tsunamis have been observed in the United States (Lander and Lockridge, 1989). Among them, the 1946 Alaskan tsunami, the 1960 Chilean tsunami and the 1964 Alaskan tsunami were recorded as three most destructive tsunamis in the United States' history. The 1946 Aleutian earthquake (Richter scale 7.3) generated a catastrophic tsunami. It attacked the Hawaiian Islands after traveling from the source region for about 5 hours and killed 159 people. The reported property damage reached $ 26 million. The 1960 Chilean tsunamis striked the Hawaiian Islands after traveling across the Pacific Ocean from the Chilean coast for 14 hours. It caused devastating damage not only along the Chilean coast, where more than 1,000 people were killed and the total property damage from the combined effects of the earthquake and tsunami was $ 417 million, but also at Hilo, Hawaii, where 61 deaths and $ 23.5 million in property damage were reported. The 1964 Alaskan tsunami triggered by the Prince William Sound earthquake (Richter scale 8.4), which was recorded as one of the largest earthquakes in the North American Continent, caused the most destructive damage in the Alaska's history. The tsunami killed 106 people and the total damage amounted to $ 84 million in Alaska.

Recently, three undersea earthquakes in the Pacific Ocean have generated devastating tsunamis (Cho, 1995). The epicenter of the 1992 Nicaragua earthquake was about 100 km off the Nicaragua coast. The second one was near Flores Island in Indonesia, which occurred on December 12, 1992. The third one was near Hokkaido Island in Japan, which striked on July 12, 1993. These earthquakes occurred near residential areas. Therefore, the damage caused by subsequent tsunamis was unusually large. Table 1.1 shows magnitudes of these earthquakes, loss of lives and observed maximum run-up heights.

An effective and economic way for the tsunami hazard mitigation planning is to construct inundation maps along those coastline vulnerable to tsunami flooding.

Table 1.1: The recent earthquakes occurred in the Pacific Ocean.

location	scale (Richter)	loss of lives	observed run-up (m)
Nicaragua	7.0	168	10
Indonesia	7.5	2,080	26
Japan	7.8	237	30

These maps should be developed based on the historical tsunami events and the projected scenarios. The developed inundation map could be used by the civil defense organizations to make evacuation plans in the event of a real tsunami attack. To produce realistic and reliable inundation estimates, it is essential to use a numerical model that calculates accurately tsunami propagation from a source region to the coastal areas of concern and the subsequent tsunami run-up and flooding. Because the establishment of safety zone along those coastline liable to tsunami attacks is only possible with the accurate information of tsunami inundation, it is very important to model the tsunami propagation and the inundation accurately and efficiently.

Only few numerical studies have been reported for the transoceanic propagation and inundation of tsunamis. Among these, Houston (1978) studied interactions of tsunamis with the Hawaiian Islands. He used a finite difference model, which solved the linear shallow-water equations, to simulate the propagation of the 1960 Chilean and the 1964 Alaskan tsunamis from the source regions to near the Hawaiian Islands. A finite element numerical model based on the Helmholtz equation was then used to calculate the interaction of tsunamis with the coastline of the Hawaiian Islands. A good agreement was observed between numerical solutions and tidal gage records at several locations. He also concluded that nonlinear and dispersive effects might not play important roles in the interaction of the 1960 Chilean and the 1964 Alaskan tsunamis with the coastline of the Hawaiian Islands.

Imamura *et al.* (1988) also studied the transoceanic propagation of both the

1960 Chilean and the 1964 Alaskan tsunamis from the source regions to the Japanese coastline. They developed a numerical model by discretizing the linear shallow-water equations with the leap-frog finite difference method. The numerical dispersion resulting from the leap-frog scheme was manipulated such that it replaced the physical dispersion of the linear Boussinesq equations. However, the numerical dispersion could not reproduce correctly the physical dispersion due to the ignorance of cross-differentiation term. Maximum run-up heights at several locations were calculated by using the Green's law and compared with tidal gage records. A reasonable agreement was observed.

Mader and Curtis (1991) investigated the propagation of both the 1946 and 1964 Alaskan tsunamis and the 1960 Chilean tsunami from the source regions to Hilo, Hawaii. In the numerical model, the nonlinear shallow-water equations were discretized with a finite difference scheme. Because calculations were performed on a personal computer, large spatial grid sizes were used; 20 min ($\approx 36\ km$) in the Pacific Ocean and 5 min ($\approx 9\ km$) near the Hawaiian Islands. The tsunami run-up at Hilo Bay was then calculated by using a 100 meter grid system. Therefore, there was an abrupt change from the large grid system to the small grid system in their numerical model. The offshore boundary of the small grid system was represented by a single point in the large grid system. Hence, the boundary condition was always uniform along the offshore boundary.

In this report, we describe a coupled models simulating a distant propagation and an associated run-up process of tsunamis, respectively. For a distant tsunami, tsunami could travel across the Pacific Ocean. Both the frequency dispersion and Coriolis force could play important roles. On the other hand, the wave slope of a typical tsunami is very small. Therefore, the nonlinear convective inertia force is not significant and can be ignored. The linear Boussinesq equations including Coriolis

4

force are adequate to describe the propagation of tsunamis (Imamura *et al.*, 1988; Liu *et al.*, 1994c). Generally, the distant propagation model requires a huge amount of computer memory size and computing time. However, these requirements have rapidly become a less problem because of the advancement of computer technology.

As tsunamis propagate into the shallow-water region, the wave amplitude increases and the wavelength decreases due to shoaling. The nonlinear convective inertia force becomes increasingly important. In the very shallow water, the bottom frictional effects become significant, while the significance of the frequency dispersion diminishes. Therefore, the nonlinear shallow-water equations including bottom frictional terms should be used in the description of the tsunami inundation. To obtain the information on the inundation area, a special treatment is required to track the location of a moving shoreline as waves rise and recede.

In next section, the linear model is presented. In the linear model, an explicit staggered leap-frog finite difference method is used to discretized the linear shallow-water equations. It is shown that finite difference solutions satisfy the linear Boussinesq equations up to the third order in terms of the grid size, if the time-step size, Δt, and the spatial grid size, Δx, are chosen according to the following relationship: $(\Delta x)^2 = 4h^2 + gh(\Delta t)^2$, where h is the water depth and g is the gravitational acceleration.

The nonlinear model is described in section 3. The nonlinear shallow-water equations including bottom friction terms are used as the governing equations. The explicit leap-frog finite difference scheme is also used to discretize the linear terms of the governing equations. The upwind difference scheme is employed to discretize the nonlinear convective inertia terms of the momentum equations. The bottom friction is modeled by using either Chezy's or Manning's formula. A simple numerical scheme derived from the continuity equation is used to track the moving shoreline.

In section 4, a multi-grid coupled model is applied to the Taiwanese tsunami occurred in 1986. The model is used to simulate the propagation of tsunamis from the source region near the Taiwanese coast. The nonlinear part in the coupled model is then used to simulate the flooding inside Hwa-Lien Harbor. The maximum inundation map at the Hwa-Lien Harbor is estimated and compared with available field observed data.

In section 5, a explanation on main program, subroutines, parameters and variables is presented. A brief manual which tells how to use this multi-grid coupled model is also described. The computer codes for the multi-grid coupled models is given in appendix.

2 Linear Model

2.1 Introduction

Most of tsunami-generating earthquakes occur in subduction zones around the Pacific Ocean rim, where the dense crust of the ocean floor dives beneath the edge of the lighter continental crust and sinks down into Earth's mantle (Folger, 1994). These subduction zones include the west coasts of North and South America, coasts of Japan, East Asia, and many Pacific island chains. A large scale tsunami may cause devastating damage not only in neighboring countries but also on far away shores. For instance, the 1960 Chilean tsunami caused severe damages not only along Chilean coastline but also at Hilo, Hawaii and along Japanese coastline. The leading tsunami arrived at the Hawaiian Islands chain after roughly 14 hours traveling and at Japanese coast after 22 hours traveling across the Pacific Ocean (Imamura *et al.*, 1988; Liu *et al.*, 1994c).

A tsunami may have an initial wavelength of several tens to hundreds of km. The nonlinear convective and bottom friction terms are relatively small and can be ignored, while frequency dispersion effects are depending on the wavelength and could be included in the governing equations of the linear model.

2.2 Governing Equations

The nonlinear effect is insignificant, while the frequency dispersion effect could be significant for shorter waves. Therefore, a distant propagation of tsunamis can be adequately modeled using the linear Boussinesq equations (Imamura *et al.*, 1988; Kajiura and Shuto, 1990; Liu *et al.*, 1994c). Furthermore, a tsunami travels across the ocean from the source region to the coastal region where the water depth is relatively shallower, two sets of governing equations are employed to simulate the transoceanic propagation, i.e., the linear Boussinesq equations in terms of both the

7

spherical and the Cartesian coordinate systems. After neglecting nonlinear terms, we have the following linear Boussinesq equations in the spherical coordinate system as:

$$\frac{\partial \zeta}{\partial t} + \frac{1}{R\cos\varphi}\left[\frac{\partial P}{\partial \psi} + \frac{\partial}{\partial \varphi}\left(\cos\varphi Q\right)\right] = 0 \tag{2.1}$$

$$\frac{\partial P}{\partial t} + \frac{gh}{R\cos\varphi}\frac{\partial \zeta}{\partial \psi} - fQ$$
$$= \frac{1}{R\cos\varphi}\frac{\partial}{\partial \psi}\left[\frac{h^3}{3R\cos\varphi}\frac{\partial}{\partial t}\left\{\frac{\partial}{\partial \psi}\left(\frac{P}{h}\right) + \frac{\partial}{\partial \varphi}\left(\cos\varphi\frac{Q}{h}\right)\right\}\right] \tag{2.2}$$

$$\frac{\partial Q}{\partial t} + \frac{gh}{R}\frac{\partial \zeta}{\partial \varphi} + fP$$
$$= \frac{1}{R}\frac{\partial}{\partial \varphi}\left[\frac{h^3}{3R\cos\varphi}\frac{\partial}{\partial t}\left\{\frac{\partial}{\partial \psi}\left(\frac{P}{h}\right) + \frac{\partial}{\partial \varphi}\left(\cos\varphi\frac{Q}{h}\right)\right\}\right] \tag{2.3}$$

in which (ψ, φ) denote the longitude and the latitude of the Earth. Eliminating P and Q from equations (2.1) - (2.3), the following equation can be obtained in terms of ζ without considering the Coriolis force terms.

$$\frac{\partial^2 \zeta}{\partial t^2} - \frac{gh}{R^2\cos^2\varphi}\left[\frac{\partial^2\zeta}{\partial\psi^2} + \cos\varphi\frac{\partial}{\partial\varphi}\left(\cos\varphi\frac{\partial\zeta}{\partial\varphi}\right)\right]$$
$$= \frac{gh^3}{3R^4\cos^4\varphi}\frac{\partial^4\zeta}{\partial\psi^4} + \frac{gh^3}{3R^4\cos\varphi}\frac{\partial}{\partial\varphi}\left[\cos\varphi\frac{\partial}{\partial\varphi}\left\{\frac{1}{\cos\varphi}\frac{\partial}{\partial\varphi}\left(\cos\varphi\frac{\partial\zeta}{\partial\varphi}\right)\right\}\right]$$
$$+ \frac{gh^3}{3R^4\cos^3\varphi}\left[\frac{\partial^3}{\partial\psi^2\partial\varphi}\left(\cos\varphi\frac{\partial\zeta}{\partial\varphi}\right) + \cos^2\varphi\frac{\partial}{\partial\varphi}\left\{\cos\varphi\frac{\partial}{\partial\varphi}\left(\frac{1}{\cos^2\varphi}\frac{\partial^2\zeta}{\partial\psi^2}\right)\right\}\right] \tag{2.4}$$

where the water depth is assumed to be constant

For a smaller scale computation, a local Cartesian coordinate system can be used. After neglecting nonlinear terms from the Boussinesq equations, the linear Boussinesq equations can also be obtained in the Cartesian coordinate system as:

$$\frac{\partial \zeta}{\partial t} + \frac{\partial P}{\partial x} + \frac{\partial Q}{\partial y} = 0 \tag{2.5}$$

$$\frac{\partial P}{\partial t} + gh\frac{\partial \zeta}{\partial x} = \frac{h^2}{2}\frac{\partial}{\partial x}\left[\frac{\partial}{\partial x}\left(\frac{\partial P}{\partial t}\right) + \frac{\partial}{\partial y}\left(\frac{\partial Q}{\partial t}\right)\right]$$
$$- \frac{h^3}{6}\frac{\partial}{\partial x}\left[\frac{\partial^2}{\partial t\partial x}\left(\frac{P}{h}\right) + \frac{\partial^2}{\partial t\partial y}\left(\frac{Q}{h}\right)\right] \tag{2.6}$$

8

$$\frac{\partial Q}{\partial t} + gh\frac{\partial \zeta}{\partial y} = \frac{h^2}{2}\frac{\partial}{\partial y}\left[\frac{\partial}{\partial x}\left(\frac{\partial P}{\partial t}\right) + \frac{\partial}{\partial y}\left(\frac{\partial Q}{\partial t}\right)\right]$$
$$- \frac{h^3}{6}\frac{\partial}{\partial y}\left[\frac{\partial^2}{\partial t\partial x}\left(\frac{P}{h}\right) + \frac{\partial^2}{\partial t\partial y}\left(\frac{Q}{h}\right)\right] \qquad (2.7)$$

In the momentum equations (2.6) and (2.7), the Coriolis effects are also not considered. Eliminating P and Q from equations (2.5) - (2.7), the following equation can be obtained in terms of ζ.

$$\frac{\partial^2 \zeta}{\partial t^2} - g\frac{\partial}{\partial x}\left(h\frac{\partial \zeta}{\partial x}\right) - g\frac{\partial}{\partial y}\left(h\frac{\partial \zeta}{\partial y}\right)$$
$$= \frac{\partial}{\partial x}\left[\frac{h^2}{2}\frac{\partial}{\partial x}\left\{\frac{\partial}{\partial x}\left(h\frac{\partial \zeta}{\partial x}\right) + \frac{\partial}{\partial y}\left(h\frac{\partial \zeta}{\partial y}\right)\right\}\right] - \frac{\partial}{\partial x}\left[\frac{h^3}{6}\frac{\partial}{\partial x}\left(\frac{\partial^2 \zeta}{\partial x^2} + \frac{\partial^2 \zeta}{\partial y^2}\right)\right]$$
$$+ \frac{\partial}{\partial y}\left[\frac{h^2}{2}\frac{\partial}{\partial y}\left\{\frac{\partial}{\partial x}\left(h\frac{\partial \zeta}{\partial x}\right) + \frac{\partial}{\partial y}\left(h\frac{\partial \zeta}{\partial y}\right)\right\}\right] - \frac{\partial}{\partial y}\left[\frac{h^3}{6}\frac{\partial}{\partial y}\left(\frac{\partial^2 \zeta}{\partial x^2} + \frac{\partial^2 \zeta}{\partial y^2}\right)\right] \qquad (2.8)$$

For the constant water depth case, equation (2.8) can be simplified to be

$$\frac{\partial^2 \zeta}{\partial t^2} - gh\left(\frac{\partial^2 \zeta}{\partial x^2} + \frac{\partial^2 \zeta}{\partial y^2}\right) = \frac{gh^3}{3}\left(\frac{\partial^4 \zeta}{\partial x^4} + 2\frac{\partial^4 \zeta}{\partial x^2\partial y^2} + \frac{\partial^4 \zeta}{\partial y^4}\right) \qquad (2.9)$$

The fourth-order derivatives in equations (2.4) and (2.9) are frequency dispersion terms. If they are ignored, the linear Boussinesq equation is reduced to the wave equation, which can be derived directly from the linear shallow-water equations.

2.3 Finite Difference Scheme

Equations given in (2.1) - (2.3) and (2.5) - (2.7) are difficult to solve with finite difference scheme due to higher order derivative terms representing the frequency dispersion. In this study, the leap-frog finite difference scheme is used to solve the linear shallow-water equations, i.e. without frequency dispersion terms. The numerical scheme is simple and has the second-order accuracy (Imamura and Goto, 1988; Kowalik, 1993).

In general, the leap-frog scheme has a truncation error of $O((\Delta x)^2, (\Delta y)^2, (\Delta t)^2)$ and is stable if the Courant condition satisfies. In the modified equation of the

9

leap-frog scheme (Warming and Hyett, 1974), the leading error term is given by the third-order derivative form and hence the solution may predominantly show dispersive errors. However, the leap-frog scheme contains no even derivative error in the modified equation, so that the solution is not dissipative. In this study, the numerical dispersion resulting from the numerical discretization of the leap-frog finite difference scheme is manipulated to mimic the frequency dispersion of the linear Boussinesq equations.

In this report, the following corrected finite difference equations are proposed (Abbott *et al.*, 1981; Cho, 1995):

$$\frac{\zeta_{i,j}^{n+1/2} - \zeta_{i,j}^{n-1/2}}{\Delta t} + \frac{P_{i+1/2,j}^{n} - P_{i-1/2,j}^{n}}{\Delta x} + \frac{Q_{i,j+1/2}^{n} - Q_{i,j-1/2}^{n}}{\Delta y} = 0 \qquad (2.10)$$

$$\frac{P_{i+1/2,j}^{n+1} - P_{i+1/2,j}^{n}}{\Delta t} + gh\frac{\zeta_{i+1,j}^{n+1/2} - \zeta_{i,j}^{n+1/2}}{\Delta x} + \frac{\gamma gh}{12\Delta x}$$
$$\cdot\left[(\zeta_{i+1,j+1}^{n+1/2} - 2\zeta_{i+1,j}^{n+1/2} + \zeta_{i+1,j-1}^{n+1/2}) - (\zeta_{i,j+1}^{n+1/2} - 2\zeta_{i,j}^{n+1/2} + \zeta_{i,j-1}^{n+1/2})\right] = 0 \qquad (2.11)$$

$$\frac{Q_{i,j+1/2}^{n+1} - Q_{i,j+1/2}^{n}}{\Delta t} + gh\frac{\zeta_{i,j+1}^{n+1/2} - \zeta_{i,j}^{n+1/2}}{\Delta y} + \frac{\gamma gh}{12\Delta y}$$
$$\cdot\left[(\zeta_{i+1,j+1}^{n+1/2} - 2\zeta_{i,j+1}^{n+1/2} + \zeta_{i-1,j+1}^{n+1/2}) - (\zeta_{i+1,j}^{n+1/2} - 2\zeta_{i,j}^{n+1/2} + \zeta_{i-1,j}^{n+1/2})\right] = 0 \qquad (2.12)$$

in which γ takes a value of one for the proposed scheme. On the other hand, the scheme reduces to Imamura and Goto's scheme (1988) if $\gamma = 0$. After a lengthy but straightforward algebra, the modified equation associated with the proposed scheme can be obtained for ζ as (Cho, 1995):

$$\frac{\partial^2 \zeta}{\partial t^2} - C_o^2\left(\frac{\partial^2 \zeta}{\partial x^2} + \frac{\partial^2 \zeta}{\partial y^2}\right) - C_o^2\frac{(\Delta x)^2}{12}(1 - C_r^2)\left(\frac{\partial^4 \zeta}{\partial x^4} + 2\frac{\partial^4 \zeta}{\partial x^2 \partial y^2} + \frac{\partial^4 \zeta}{\partial y^4}\right)$$
$$+ (1 - \gamma)C_o^2\frac{(\Delta x)^2}{6}\frac{\partial^4 \zeta}{\partial x^2 \partial y^2} = O\left((\Delta x)^3, (\Delta x)^2\Delta t, \Delta x(\Delta t)^2, (\Delta t)^3\right) \qquad (2.13)$$

in which a uniform grid, $\Delta x = \Delta y$, has again been used. For the proposed modified scheme, $\gamma = 1$ and the last term of equation (2.13) vanishes. The leading order terms in equation (2.13) are the same as those in the wave equation. The terms of $O((\Delta x)^2)$ and of higher order are the results of numerical discretization. If Δt and Δx are chosen according to the relationship $(\Delta x)^2 = 4h^2 + gh(\Delta t)^2$, the numerical dispersion from the modified explicit leap-frog scheme mimics the frequency dispersion of the linear Boussinesq equations. That is, we actually get numerical solutions which satisfy the Boussinesq equations by solving equations (2.10) - (2.12). Furthermore, the accuracy of the numerical scheme has been raised from second order to third order. When $\gamma = 0$, equation (2.13) is the same as that used by Imamura and Goto (1988), which does not lead to a perfect match between the modified equation and the linear Boussinesq equation (2.9), because of the appearance of the additional cross-differentiation term in equation (2.13).

From the continuity equation (2.10), the proposed leap-frog scheme calculates the free surface displacement at the (i, j) grid point on the $(n+1/2)$-th time step. These computations are fully explicit and require information on the volume flux components and the free surface displacement from the previous time step. The volume flux components are not evaluated at the same location as that for the free surface displacement. Figure 2.1 shows a grid system in which the free surface displacement is calculated at the center and the volume fluxes are obtained at the surrounding grid points, i.e., $P_{i+1/2,j}$, $P_{i-1/2,j}$, $Q_{i,j+1/2}$, and $Q_{i,j-1/2}$. The momentum equations, (2.11) and (2.12), are then used to calculate the volume flux components, $P_{i+1/2,j}^{n+1}$ and $Q_{i,j+1/2}^{n+1}$. Note that the calculations for the free surface displacement and the volume flux components are also staggered in time.
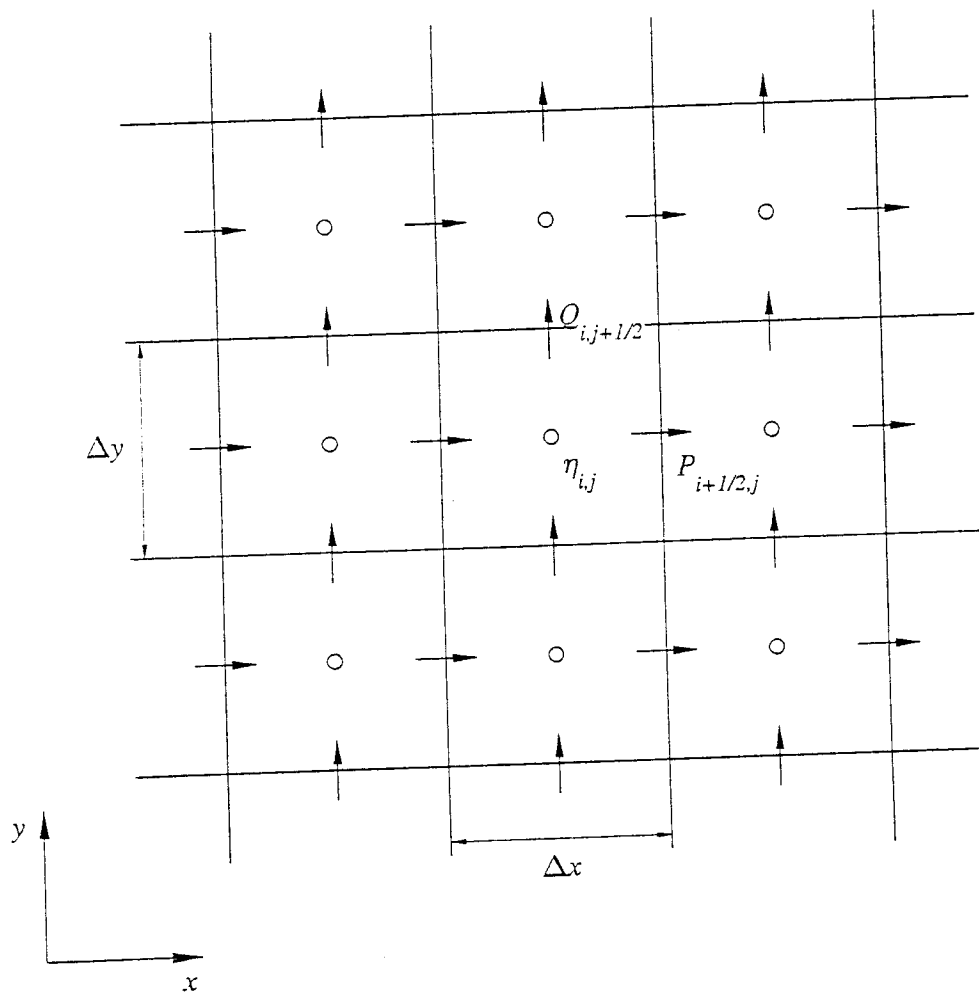
Figure 2.1: A sketch of the staggered finite difference grid system

2.4 Numerical Dispersion

In this section, the numerical dispersion generated by the proposed scheme is investigated. To determine the dispersion of the modified leap-frog finite difference scheme, a progressive wave is considered (Mei, 1989):

$$\zeta = Ae^{\hat{i}(k_x x + k_y y - \omega t)} \quad , \quad k^2 = k_x{}^2 + k_y{}^2 \tag{2.14}$$

where $\hat{i} = \sqrt{-1}$ is the unit imaginary number and k_x and k_y are x- and y-components of wave number vector $\mathbf{k}$, respectively. Substituting equation (2.14) into equation (2.13), the following relation can be derived

$$C = \frac{\omega}{k} = (gh)^{1/2} \left[1 - \frac{(kh)^2}{3} + (1 - \gamma)\frac{(\Delta x)^2}{6} \left(\frac{k_x k_y}{k} \right)^2 \right]^{1/2} \tag{2.15}$$

Once again when $\gamma = 1$ (i.e., the modified explicit leap-frog method is used) the dispersion relationship (2.15) becomes the same as that derived from the linear Boussinesq equation, that is

$$C = \frac{\omega}{k} = (gh)^{1/2} \left[1 - \frac{(kh)^2}{3} \right]^{1/2} \tag{2.16}$$

For one-dimensional problems with waves traveling in the either x- or y-direction, i.e., either k_y or k_x equals to zero, both explicit schemes yield the same phase velocity as that produced by the linear Boussinesq equations. For obliquely traveling waves, however, the phase velocity is faster than that of the linear Boussinesq equations when $\gamma = 0$ and the largest discrepancy occurs when waves propagate in the direction of $(2n + 1)\frac{\pi}{4}$, $n = 0, 1, 2, ...$, with respect to the x-axis.

2.5 Stability Analysis

In this section, the stability condition is determined for the numerical algorithms given in equations (2.10) - (2.12). Assuming that solutions for these equations can

be written in the following Fourier forms (Lapidus and Pinder, 1982):

$$\zeta = \zeta_\circ \rho^t e^{\hat{i}k_x x} e^{\hat{i}k_y y} \tag{2.17}$$

$$P = P_\circ \rho^t e^{\hat{i}k_x x} e^{\hat{i}k_y y} \tag{2.18}$$

$$Q = Q_\circ \rho^t e^{\hat{i}k_x x} e^{\hat{i}k_y y} \tag{2.19}$$

in which $\zeta_\circ$, $P_\circ$ and $Q_\circ$ are initial values of ζ, P and Q, respectively. We look for the stability condition which requires that the absolute value of amplification factor, $|\rho^{\Delta t}|$, is less than or equal to unity. Substituting equations (2.17) - (2.19) into equations (2.10) - (2.12) and using the following notation: $t = n_\circ \Delta t$ ($n_\circ = 0, 1, 2, ..., n, ...$), $x = i_\circ \Delta x$ ($i_\circ = 0, 1, 2, ..., i, ...$), and $y = j_\circ \Delta y$ ($j_\circ = 0, 1, 2, ..., j, ...$), we obtain

$$(\rho^{\Delta t/2} - \rho^{-\Delta t/2})\zeta_\circ + 2\hat{i}r_x \sin\theta_x P_\circ + 2\hat{i}r_y \sin\theta_y Q_\circ = 0 \tag{2.20}$$

$$\frac{2\hat{i}}{3}C_\circ^2 r_x \sin\theta_x (3 - \gamma \sin^2\theta_y)\rho^{\Delta t/2}\zeta_\circ + (\rho^{\Delta t} - 1)P_\circ = 0 \tag{2.21}$$

$$\frac{2\hat{i}}{3}C_\circ^2 r_y \sin\theta_y (3 - \gamma \sin^2\theta_x)\rho^{\Delta t/2}\zeta_\circ + (\rho^{\Delta t} - 1)Q_\circ = 0 \tag{2.22}$$

where the following notations have been used for simplicity

$$r_x = \frac{\Delta t}{\Delta x}, \quad r_y = \frac{\Delta t}{\Delta y}, \quad \theta_x = \frac{k_x \Delta x}{2}, \quad \theta_y = \frac{k_y \Delta y}{2}.$$

Equations (2.20) - (2.22) can be rewritten in a matrix form as:

$$\begin{bmatrix} \rho^{\Delta t/2} - \rho^{-\Delta t/2} & 2\hat{i}r_x \sin\theta_x & 2\hat{i}r_y \sin\theta_y \\ \frac{2\hat{i}}{3}ghr_x \sin\theta_x(3 - \sin^2\theta_y)\rho^{\Delta t/2} & \rho^{\Delta t} - 1 & 0 \\ \frac{2\hat{i}}{3}ghr_y \sin\theta_y(3 - \sin^2\theta_x)\rho^{\Delta t/2} & 0 & \rho^{\Delta t} - 1 \end{bmatrix} \begin{Bmatrix} \zeta_\circ \\ P_\circ \\ Q_\circ \end{Bmatrix} = 0 \tag{2.23}$$

The system of linear equations given in equations (2.20) - (2.22) is homogeneous. For nontrivial solutions, the determinant of the coefficient matrix (2.23) must vanish. Consequently, two equations can be found for the amplification factor, $\rho^{\Delta t}$, as:

$$\rho^{\Delta t/2} - \rho^{-\Delta t/2} = 0 \tag{2.24}$$

$$(\rho^{\Delta t}-1)^2 + \frac{4}{3}C_\circ^2\left[r_x^2\sin^2\theta_x(3-\gamma\sin^2\theta_y) + r_y^2\sin^2\theta_y(3-\gamma\sin^2\theta_x)\right]\rho^{\Delta t} = 0 \tag{2.25}$$

Obviously, $\rho^{\Delta t} = 1$ is the solution of equation (2.24). From equation (2.25), the amplification factor can be determined as

$$\rho^{\Delta t} = \frac{2 - \Gamma \pm (\Gamma^2 - 4\Gamma)^{1/2}}{2} \tag{2.26}$$

where Γ is given by

$$\Gamma = \frac{4}{3}C_\circ^2\left[r_x^2\sin^2\theta_x(3 - \gamma\sin^2\theta_y) + r_y^2\sin^2\theta_y(3 - \gamma\sin^2\theta_x)\right] \tag{2.27}$$

The stability condition

$$|\rho^{\Delta t}| \leq 1 \tag{2.28}$$

is satisfied, if $\Gamma^2 - 4\Gamma$ is less than or equal to zero, i.e.,

$$0 \leq \Gamma \leq 4 \tag{2.29}$$

Substituting equation (2.27) into equation (2.29) and assuming that $\Delta x = \Delta y$ for simplicity, we obtain

$$C_r \leq \frac{3^{1/2}}{\left[\sin^2\theta_x(3 - \gamma\sin^2\theta_y) + \sin^2\theta_y(3 - \gamma\sin^2\theta_x)\right]^{1/2}} \tag{2.30}$$

where C_r is the Courant number. If Imamura and Goto's explicit scheme is used ($\gamma = 0$), the stability condition can be simplified to be

$$C_r \leq \frac{1}{\left[\sin^2\theta_x + \sin^2\theta_y\right]^{1/2}} \tag{2.31}$$

15

The largest allowable Courant number is 0.7071 when $\sin \theta_x = \sin \theta_y = 1$ for the $\gamma = 0$ case. On the other hand, if the modified explicit scheme is used ($\gamma = 1$), the largest Courant number is 0.8660. Therefore, for the same Δx and C_o values, the modified explicit scheme allows slightly larger time-step size than that required by Imamura and Goto's scheme. For a one-dimensional case, C_r for both schemes becomes the usual stability condition for an explicit scheme; that is, C_r less than or equal to one.

3 Nonlinear Model

3.1 Introduction

In the previous section, linear shallow-water equations are used to simulate a distant propagation of tsunamis. The numerical dispersion has been manipulated to mimic the frequency dispersion of the linear Boussinesq equations.

As the tsunami propagates over a continental shelf and approaches a coastal area, linear shallow-water equations are no longer valid. The wavelength of the incident tsunami becomes shorter and the amplitude becomes larger as the leading wave of a tsunami propagates into shallower water. Therefore the nonlinear convective inertia force and bottom friction terms become increasingly important, while the significance of the Coriolis force and the frequency dispersion terms diminishes. The nonlinear shallow-water equations including bottom frictional effects are adequate to describe the flow motion in the coastal zone (Kajiura and Shuto, 1990; Liu *et al.*, 1994c). Furthermore, along the shoreline, where the water depth becomes zero, a special treatment is required to properly track shoreline movements.

3.2 Governing Equations

The nonlinear shallow-water equations including bottom frictional effects can be written as:

$$\frac{\partial \zeta}{\partial t} + \frac{\partial P}{\partial x} + \frac{\partial Q}{\partial y} = 0 \tag{3.1}$$

$$\frac{\partial P}{\partial t} + \frac{\partial}{\partial x}\left(\frac{P^2}{H}\right) + \frac{\partial}{\partial y}\left(\frac{PQ}{H}\right) + gH\frac{\partial \zeta}{\partial x} + \tau_x H = 0 \tag{3.2}$$

$$\frac{\partial Q}{\partial t} + \frac{\partial}{\partial x}\left(\frac{PQ}{H}\right) + \frac{\partial}{\partial y}\left(\frac{Q^2}{H}\right) + gH\frac{\partial \zeta}{\partial y} + \tau_y H = 0 \tag{3.3}$$

17

Bottom frictional terms can be modeled by using either Chezy's formula or Manning's formula, i.e., for the Chezy's formula

$$\tau_x = \frac{g}{C_f^2 H^3} P \left(P^2 + Q^2 \right)^{1/2}, \quad \tau_y = \frac{g}{C_f^2 H^3} Q \left(P^2 + Q^2 \right)^{1/2} \tag{3.4}$$

in which C_f is the Chezy's frictional coefficient, and for the Manning's formula

$$\tau_x = \frac{gn^2}{H^{10/3}} P \left(P^2 + Q^2 \right)^{1/2}, \quad \tau_y = \frac{gn^2}{H^{10/3}} Q \left(P^2 + Q^2 \right)^{1/2} \tag{3.5}$$

where n is the Manning's relative roughness coefficient. Both empirical constants, n and C_f, are dependent of the flow condition, i.e., the Reynolds number and the surface roughness of the beach.

3.3 Finite Difference Scheme

The nonlinear shallow-water equations, (3.1) - (3.3), are discretized by using the leap-frog finite difference scheme used in the linear model (i.e. equations (2.10) - (2.12)). The nonlinear convective terms are discretized with an upwind scheme. In general, the upwind scheme is conditionally stable and introduces some numerical dissipation. But if the velocity gradient in the fluid field is not too steep and if the stability condition, which is $\sqrt{gh} * \Delta t / \Delta x < 1$, is satisfied, upwind formulation is preferred for solving advective terms since, at each time step, only a small computational effort is required.

The linear terms of the governing equations are also discretized by the leap-frog finite difference scheme. The nonlinear convective terms of the momentum equations are discretized by using an upwind scheme and given as:

$$\frac{\partial}{\partial x} \left(\frac{P^2}{H} \right) = \frac{1}{\Delta x} \left[\lambda_{11} \frac{\left(P_{i+3/2,j}^n \right)^2}{H_{i+3/2,j}^n} + \lambda_{12} \frac{\left(P_{i+1/2,j}^n \right)^2}{H_{i+1/2,j}^n} + \lambda_{13} \frac{\left(P_{i-1/2,j}^n \right)^2}{H_{i-1/2,j}^n} \right] \tag{3.6}$$

$$\frac{\partial}{\partial y} \left(\frac{PQ}{H} \right) = \frac{1}{\Delta y} \left[\lambda_{21} \frac{(PQ)_{i+1/2,j+1}^n}{H_{i+1/2,j+1}^n} + \lambda_{22} \frac{(PQ)_{i+1/2,j}^n}{H_{i+1/2,j}^n} + \lambda_{23} \frac{(PQ)_{i+1/2,j-1}^n}{H_{i+1/2,j-1}^n} \right] \tag{3.7}$$

18

$$\frac{\partial}{\partial x}\left(\frac{PQ}{H}\right) = \frac{1}{\Delta x}\left[\lambda_{31}\frac{(PQ)^n_{i+1,j+1/2}}{H^n_{i+1,j+1/2}} + \lambda_{32}\frac{(PQ)^n_{i,j+1/2}}{H^n_{i,j+1/2}} + \lambda_{33}\frac{(PQ)^n_{i-1,j+1/2}}{H^n_{i-1,j+1/2}}\right] \qquad (3.8)$$

$$\frac{\partial}{\partial y}\left(\frac{Q^2}{H}\right) = \frac{1}{\Delta y}\left[\lambda_{41}\frac{\left(Q^n_{i,j+3/2}\right)^2}{H^n_{i,j+3/2}} + \lambda_{42}\frac{\left(Q^n_{i,j+1/2}\right)^2}{H^n_{i,j+1/2}} + \lambda_{43}\frac{\left(Q^n_{i,j-1/2}\right)^2}{H^n_{i,j-1/2}}\right] \qquad (3.9)$$

In equations (3.6) - (3.9), coefficients, λ, are determined from

$$\left[\begin{array}{llll} \lambda_{11} = 0, & \lambda_{12} = 1, & \lambda_{13} = -1, & \text{if } P^n_{i+1/2,j} \geq 0 \\ \lambda_{11} = 1, & \lambda_{12} = -1, & \lambda_{13} = 0, & \text{if } P^n_{i+1/2,j} < 0 \end{array}\right.$$

$$\left[\begin{array}{llll} \lambda_{21} = 0, & \lambda_{22} = 1, & \lambda_{23} = -1, & \text{if } Q^n_{i+1/2,j} \geq 0 \\ \lambda_{21} = 1, & \lambda_{22} = -1, & \lambda_{23} = 0, & \text{if } Q^n_{i+1/2,j} < 0 \end{array}\right.$$

$$\left[\begin{array}{llll} \lambda_{31} = 0, & \lambda_{32} = 1, & \lambda_{33} = -1, & \text{if } P^n_{i,j+1/2} \geq 0 \\ \lambda_{31} = 1, & \lambda_{32} = -1, & \lambda_{33} = 0, & \text{if } P^n_{i,j+1/2} < 0 \end{array}\right.$$

$$\left[\begin{array}{llll} \lambda_{41} = 0, & \lambda_{42} = 1, & \lambda_{43} = -1, & \text{if } Q^n_{i,j+1/2} \geq 0 \\ \lambda_{41} = 1, & \lambda_{42} = -1, & \lambda_{43} = 0, & \text{if } Q^n_{i,j+1/2} < 0 \end{array}\right.$$

Since the upwind scheme is employed, the discretized momentum equations are only first order in accuracy in terms of spatial grid sizes. Bottom frictional terms are discretized as

$$\tau_x H = \nu_x \left(P^{n+1}_{i+1/2,j} + P^n_{i+1/2,j}\right) \qquad (3.10)$$

$$\tau_y H = \nu_y \left(Q^{n+1}_{i,j+1/2} + Q^n_{i,j+1/2}\right) \qquad (3.11)$$

in which ν_x and ν_y are given by

$$\nu_x = \frac{1}{2}\frac{g}{C_f^2\left(H^n_{i+1/2,j}\right)^2}\left[\left(P^n_{i+1/2,j}\right)^2 + \left(Q^n_{i+1/2,j}\right)^2\right]^{1/2}$$

$$\nu_y = \frac{1}{2}\frac{g}{C_f^2\left(H^n_{i,j+1/2}\right)^2}\left[\left(P^n_{i,j+1/2}\right)^2 + \left(Q^n_{i,j+1/2}\right)^2\right]^{1/2}$$

for the Chezy's formula, and

$$\nu_x = \frac{1}{2} \frac{gn^2}{\left(H_{i+1/2,j}^n\right)^{7/3}} \left[\left(P_{i+1/2,j}^n\right)^2 + \left(Q_{i+1/2,j}^n\right)^2\right]^{1/2}$$

$$\nu_y = \frac{1}{2} \frac{gn^2}{\left(H_{i,j+1/2}^n\right)^{7/3}} \left[\left(P_{i,j+1/2}^n\right)^2 + \left(Q_{i,j+1/2}^n\right)^2\right]^{1/2}$$

for the Manning's formula. Finally, finite difference forms for the continuity and momentum equations are written as

$$\zeta_{i,j}^{n+1/2} = \zeta_{i,j}^{n-1/2} - r_x\left(P_{i+1/2,j}^n - P_{i-1/2,j}^n\right) - r_y\left(Q_{i,j+1/2}^n - Q_{i,j-1/2}^n\right) \qquad (3.12)$$

$$P_{i+1/2,j}^{n+1} = \frac{1}{1+\nu_x\Delta t}\left[(1-\nu_x\Delta t)P_{i+1/2,j}^n - r_x g H_{i+1/2,j}^{n+1/2}\left(\zeta_{i+1,j}^{n+1/2} - \zeta_{i,j}^{n+1/2}\right)\right]$$

$$- \frac{r_x}{1+\nu_x\Delta t}\left[\lambda_{11}\frac{\left(P_{i+3/2,j}^n\right)^2}{H_{i+3/2,j}^n} + \lambda_{12}\frac{\left(P_{i+1/2,j}^n\right)^2}{H_{i+1/2,j}^n} + \lambda_{13}\frac{\left(P_{i-1/2,j}^n\right)^2}{H_{i-1/2,j}^n}\right]$$

$$- \frac{r_y}{1+\nu_x\Delta t}\left[\lambda_{21}\frac{(PQ)_{i+1/2,j+1}^n}{H_{i+1/2,j+1}^n} + \lambda_{22}\frac{(PQ)_{i+1/2,j}^n}{H_{i+1/2,j}^n} + \lambda_{23}\frac{(PQ)_{i+1/2,j-1}^n}{H_{i+1/2,j-1}^n}\right] \qquad (3.13)$$

$$Q_{i,j+1/2}^{n+1} = \frac{1}{1+\nu_y\Delta t}\left[(1-\nu_y\Delta t)Q_{i,j+1/2}^n - r_y g H_{i,j+1/2}^{n+1/2}\left(\zeta_{i,j+1}^{n+1/2} - \zeta_{i,j}^{n+1/2}\right)\right]$$

$$- \frac{r_x}{1+\nu_y\Delta t}\left[\lambda_{31}\frac{(PQ)_{i+1,j+1/2}^n}{H_{i+1,j+1/2}^n} + \lambda_{32}\frac{(PQ)_{i,j+1/2}^n}{H_{i,j+1/2}^n} + \lambda_{33}\frac{(PQ)_{i-1,j+1/2}^n}{H_{i-1,j+1/2}^n}\right]$$

$$- \frac{r_y}{1+\nu_y\Delta t}\left[\lambda_{41}\frac{\left(Q_{i,j+3/2}^n\right)^2}{H_{i,j+3/2}^n} + \lambda_{42}\frac{\left(Q_{i,j+1/2}^n\right)^2}{H_{i,j+1/2}^n} + \lambda_{43}\frac{\left(Q_{i,j-1/2}^n\right)^2}{H_{i,j-1/2}^n}\right] \qquad (3.14)$$

in which $r_x = \Delta t/\Delta x$ and $r_y = \Delta t/\Delta y$. Following approximations have been used to derive finite difference equations (3.12) - (3.14).

$$H_{i+1/2,j}^{n+1/2} = \frac{1}{2}\left(H_{i,j}^{n+1/2} + H_{i+1,j}^{n+1/2}\right) \qquad (3.15)$$

$$H_{i,j+1/2}^{n+1/2} = \frac{1}{2}\left(H_{i,j}^{n+1/2} + H_{i,j+1}^{n+1/2}\right) \qquad (3.16)$$

$$H_{i+1/2,j}^n = \frac{1}{4} \left(H_{i,j}^{n-1/2} + H_{i,j}^{n+1/2} + H_{i+1,j}^{n-1/2} + H_{i+1,j}^{n+1/2} \right) \qquad (3.17)$$

$$H_{i,j+1/2}^n = \frac{1}{4} \left(H_{i,j}^{n-1/2} + H_{i,j}^{n+1/2} + H_{i,j+1}^{n-1/2} + H_{i,j+1}^{n+1/2} \right) \qquad (3.18)$$

$$P_{i,j+1/2}^n = \frac{1}{4} \left(P_{i-1/2,j}^n + P_{i-1/2,j+1}^n + P_{i+1/2,j}^n + P_{i+1/2,j+1}^n \right) \qquad (3.19)$$

$$Q_{i+1/2,j}^n = \frac{1}{4} \left(Q_{i,j-1/2}^n + Q_{i+1,j-1/2}^n + Q_{i,j+1/2}^n + Q_{i+1,j+1/2}^n \right) \qquad (3.20)$$

3.4 Moving Boundary Condition

In carrying out numerical computations, the computational domain is divided into finite difference grids. Initially, the free surface displacement is zero everywhere, as are the volume fluxes. When the grid point is on dry land, the "water depth," h, takes a negative value and gives the elevation of the land measured from the mean water level. Figure 3.1 shows a schematic sketch of the moving boundary treatment used in the study. The MWL represents the mean water level and H_f denotes the flooding depth in figure 3.1. In a land (dry) cell the total depth, $H = h + \zeta$, has a negative value. On the other hand, the wet cell has a positive H value. The interface between the dry cells and wet cells defines the shoreline. The continuity equation in conjunction with boundary conditions along offshore boundaries is used to find free surface displacements at the next time step in the entire computational domain, including the dry (land) cells. The free surface displacement at a dry land grid remains zero because the volume fluxes are zero at the neighboring grid points (see figure 2.1). At a shoreline grid, the total depth, H, is updated. A numerical algorithm is needed to determine if the total water depth is high enough to flood the neighboring dry (land) cells and hence to move the shoreline. The momentum equations are used to update the volume fluxes in the wet cells only.

21

To illustrate the moving boundary algorithm, the one-dimensional case is used as an example. As shown in figure 3.1, the real bathymetry has been replaced by a staircase representation. The total depth, H, is calculated and recorded at grid points $i-1$, i and $i+1$, while the volume flux is computed at grid points $i-1/2$, $i+1/2$ and $i+3/2$. As shown in figure 3.1 (a), the i-th cell is a wet cell in which the total depth is positive and the $i+1$-th cell is a dry (land) cell in which the total depth is negative and the volume fluxes are zero. The shoreline is somewhere between the i-th and the $i+1$-th grid points. Then, the volume flux at the $i+1/2$-th grid point is assigned to be zero. Therefore, the shoreline does not move to the on-shore direction. When the water surface is rising as shown in figure 3.1 (b), however, the volume flux at the $i+1/2$-th grid point is no longer zero. The shoreline may move one grid point to the on-shore direction. After the total depth has been updated from the continuity equation, the following algorithm is used to determine whether or not the shoreline should be moved. If $H_i > 0$, possible cases can be summarized as

- If $H_{i+1} \leq 0$ and $h_{i+1} + \zeta_i \leq 0$, then the shoreline remains between grid points i and $i + 1$ and the volume flux $P_{i+1/2}$ remains zero.

- If $H_{i+1} \leq 0$ and $h_{i+1} + \zeta_i > 0$, then the shoreline moves to between grid points $i+1$ and $i+2$. The volume flux $P_{i+1/2}$ may have a nonzero value, while $P_{i+3/2}$ is assigned to be zero. The flooding depth is $H_f = h_{i+1} + \zeta_i$.

- If $H_{i+1} > 0$, then the shoreline moves to between grid points $i+1$ and $i+2$. The volume flux $P_{i+1/2}$ may also have a nonzero value, while $P_{i+3/2}$ has a zero value. The flooding depth is $H_f = \max\left(h_{i+1} + \zeta_i, h_{i+1} + \zeta_{i+1}\right)$.

In the above cases, the time-step index has been omitted for simplicity. The algorithm is developed for a two-dimensional problem and the corresponding y-direction algorithm has the same procedure as that for the x-direction.

To save computing time, the regions that represent permanent dry (land) can be excluded from the computation by installing a depth criterion. Moreover, when H is very small, the associated bottom friction term become very large and, accordingly, a lower bound of the water depth is used to avoid the difficulty. The finite difference approximation for the continuity equation correctly accounts for positive and zero values of the total depth on each side of a computational grid. The treatment of flooding and ebbing grid cells guarantees mass conservation while accounting for the flooding and ebbing of land. The occurrence of a zero value for the total depth H on one side of a cell implies zero mass flux until H becomes positive. A grid cell is considered a dry cell only if the total water depths at all sides are zero or negative.
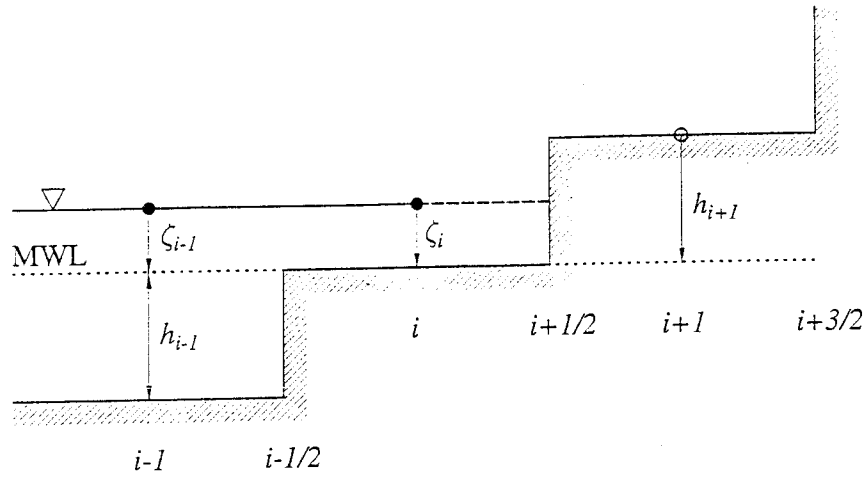
(a) case 1
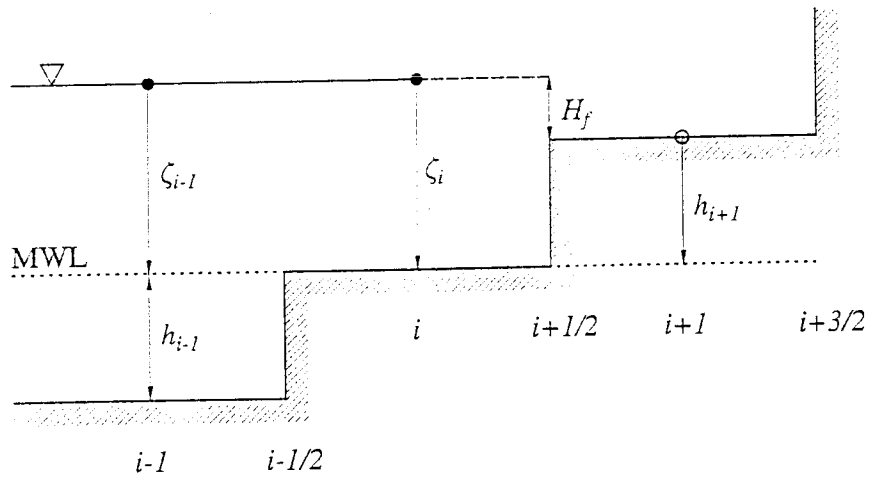
(b) case 2

Figure 3.1: A schematic sketch of the moving boundary treatment

24

4 Multi-Grid Coupled Model

4.1 Introduction

There are several reasons for applying the nested multi-grid model. When the water depth varies within the computational domain, it might be desirable that different grid size and time step size be employed in different subregions so that the frequency dispersion is adequately represented. On the other hand, offenly we would like to obtain detailed information in the coastal region. Finer grids should be used only in certain specific regions.

In the present model either the linear or the nonlinear version of shallow-water equation with different subcoordinate system (i.e. Cartesian or Spherical) can be assigned to a specific subregion. These subregions are dynamically connected. The model has also been designed so that any ratio of grid sizes between two adjacent subregions can be used.

4.2 Connecting Boundary Condition

We briefly describe the technique for exchanging information between two subregions of different grid sizes. As shown in figure 4.1, a smaller grid system is nested in a larger grid system with the ratio of 1:3. The arrows represent the volume fluxes, P and Q, across each grid cell, while circles and dots indicate the locations where the free surface displacement is evaluated.

At a certain time level, volume fluxes in both large and small grid systems are determined from the momentum equations, with the exception of volume fluxes for the smaller grid system along the boundaries between two subregions. These data are determined by interpolating the neighboring volume fluxes from the large grid system. The free surface displacement at the next time level for the small grid system can be calculated from the continuity equation. Usually the time step size for the

smaller grid system is also smaller than that used in the larger grid system to satisfy the CFL (Courant-Friedrichs-Lewy) condition, which is $c*dt/dx < 1$. Therefore, the volume fluxes along the boundary of the small grid system at the next time level must be obtained by interpolating the neighboring volume fluxes obtained from the large grid system over a larger time interval. After the free surface displacements in the small grid system are calculated up to the next time level of the large grid system, the free surface displacements in the large grid system are updated by solving the continuity equation.

Let us describe these procedures step by step. Suppose all flux values in the inner and the outer region are known at time level $t = t_1$. And we need to solve the inner and the outer region values at the next time step $t = t_2$. Remember that the time step of the inner region is one half of that of the outer region.

[$STEP$ 1] Get the free surface elevation at $t_{1+1/2}$ in the outer region by solving continuity equation.

[$STEP$ 2] To solve the continuity in the inner region, however, we need to have the flux information along the connected boundary at t_1. So the flux values in the outer grid at the connected boundary are lineary interpolated and then those interpolated values are assigned to the flux in the inner grid at the boundary.

[$STEP$ 3] Get the free surface elevation at $t_{1+1/4}$ in the inner region by solving continuity equation.

[$STEP$ 4] Get the flux values at $t_{1+1/2}$ in the inner region by solving momentum equation.

[$STEP$ 5] To get the free surface elevation at $t_{1+3/4}$ in the inner region, we should have the flux information along the connected boundary at $t_{1+1/2}$. To get these information we can do in the following way. First, since we already know the free surface elevation at $t_{1+1/2}$ and flux at t_1 in the outer region, we can get the flux in

the outer region along the connected boundary at t_2 by solving linear momentum equation locally. Second, these flux values at t_2 are lineary interpolated along the connected boundary. And to get the value at $t_{1+1/2}$, outer flux values at t_1 and t_2 are time averaged. Those spatially and timely averaged flux values are assigned to the flux in the inner grid at the boundary.

[$STEP$ 6] Get the free surface elevation at $t_{1+3/4}$ in the inner region by solving continuity equation.

[$STEP$ 7] To transfer the information from the inner region to the outer region, the free surface elevation in the inner region is spatially averaged over the grid size of the outer region. These averaged elevation values at $t_{1+3/4}$ are then time averaged with those at $t_{1+1/4}$ in inner region. These spatially and timely averaged elevation values in the inner region update the elevation values at $t_{1+1/2}$ in the outer region.

[$STEP$ 8] Get the flux values at t_2 in the inner region by solving momentum equation.

[$STEP$ 9] Get the flux values at t_2 in the outer region by solving momentum equation.
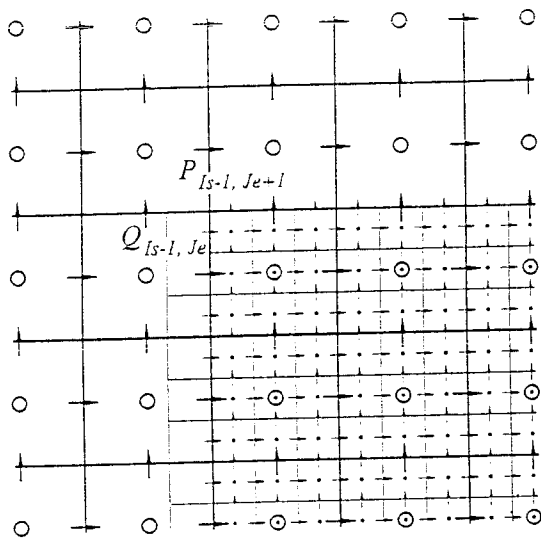
a) upper left corner
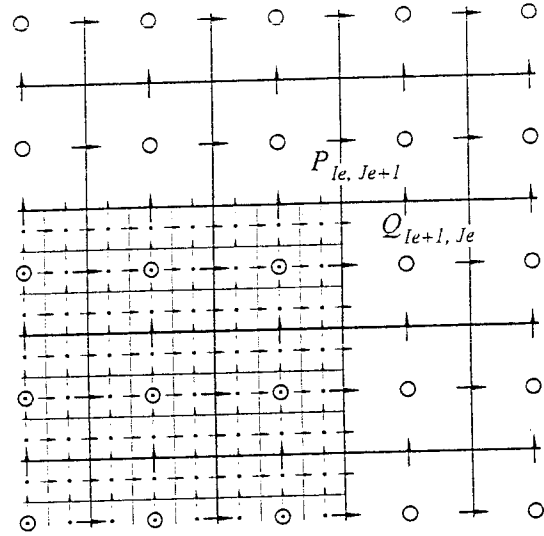
b) upper right corner
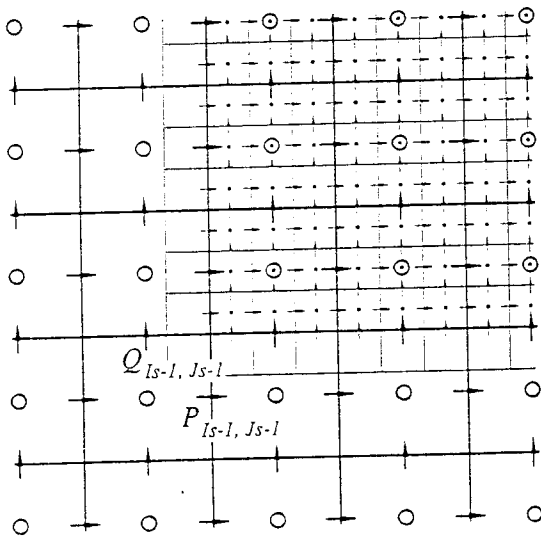
c) lower left corner
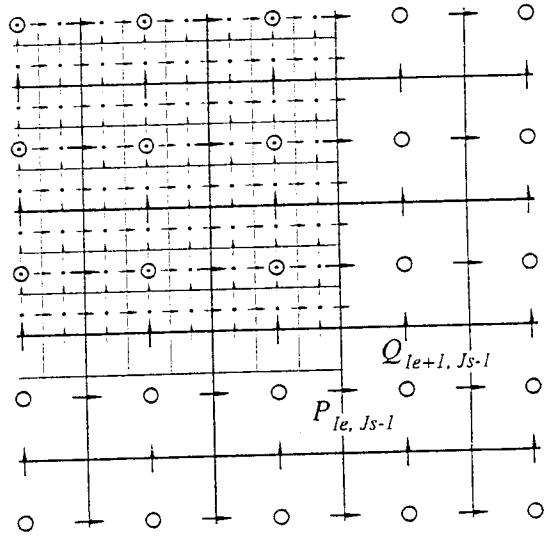
d) lower right corner

Figure 4.1: Connecting boundary between two subregion

4.3 Numerical Example

Since the linear and nonlinear components of the model have been verified previously in terms of numerical accuracy and stability (Cho, 95), the most critical element in the present nested model is the stability of the numerical scheme for the connecting boundary condition. To examine the connecting boundary condition, we would like to test the nested model by checking the propagation and the reflection of solitary wave across the connecting boundary.

In the case of the propagation of solitary wave over constant water depth, comparisons between the numerical solutions and the corresponding analytical solutions are made. Also, to verify the validity of the proposed scheme which enable us to use any ratio of grid sizes between two adjacent subregions, numerical solutions of the grid ratio of 1:3 and 1:5 is compared.

4.3.1 Propagation of Solitary Wave

In the first example, we would like to check our nested grid model by investigating the propagation of solitary wave over constant depth. To simulate a solitary wave, which could exist only when the nonlinearity and dispersion is balanced each other precisely, we need to represent the physical dispersion. As pointed out earlier, the present model is able to replace the physical dispersion by the numerical dispersion, which is caused by the leading numerical error of the leap-frog scheme. So we should choose the grid size properly.

Figure 4.2 shows the numerical domain which is used in our test. The ratio of the grid size between adjacent domain is 1:3, so whole ratio of grid size is 1:3:9. We made another computational domain whose ratio is 1:5:25 to compare the numerical result with that of 1:3:9. Note that the region B is located from 18.4 to 96.6 in x/h coordinate and region C is from 34.5 to 78.2 By setting the inner region of high

resolution (region B and C) such as shown in figure 4.2, we could check the validity of connecting boundary condition as the wave propagates through different regions.

A sequence of snapshots of free-surface displacement for the propagation of solitary wave is shown in figure 4.3. The water depth h is $30m$, wave length is about $60h$, nonlinearity a/h is 0.01 and frequency dispersion kh is 0.1. In subsequent 3-D plots, the free surface displacement in the areas corresponding to the region B and C is plotted together with the outer regin A in order to check if there is any discontinuity of water surface in different regions. We can see that the wave propagation is very smooth and that there is no significant numerical error when the wave acrosses the boundaries of three regions of different grid resolution. In other words the connecting boundary condition seems to exchange the information between two adjacent regions very well.

Figure 4.4 shows the free surface profile along the center line (from α to β in Figure 4.2). In this plot we would like to compare the numerical results of uniform grid model with those of the nested grid model. We can expect that if the connecting boundary condition works well, the numerical result of coupled model should be exist between the result of uniform grid model of low resolution and high resolution. In figure 4.4, we can see the result of nested grid model of 1:5:25 (dx=81m:16m:3.2m) lies between the result of dx=81m and dx=16m in region C. Also the result of 1:5:25 agrees generally well with that of 1:3:9 which enable us to believe that the numerical scheme for connecting arbitrary ratio of grid size also works well. Notice that in the figure 4.4 the free surface distribution starts from $x/h = 40$ for the nested grid model where two subregions are connected.

In figure 4.5 we compare our numerical results with analytical solution with higher nonlinearity ($a/h = 0.05$). Since we introduce the numerical dispersion by choosing the grid size, if we reduce the grid size, we cannot get proper amount of dispersion

which is needed to simulate the solitary wave propagation. In other words, if we remove the numerical dispersion by making grid size too small, we cannot generate solitary wave anymore. In figure 4.5, by reducing the grid size (dx) from 81m to 16m, we can see the wave form is much steep and asymmetric compared with the analytic soluction, which tells us that in case of dx=16m, we put too little numerical dispersion. On the other hand, when the grid size is 81 m, we put too much numerical dispersion so that the oscillatory tail is generated and the leading wave amplitude is reduced. The water surface profile of the nested grid model (1:3:9) located between the results of the uniform grid model of dx:81m and dx:16m, which is less dispersive than the coarse unifom grid model result and wave steepness is milder than that of the fine uniform grid model. It is resonable result because in nested grid region the grid size is smaller than the coarse uniform grid (dx=81m) and larger than the fine uniform grid (dx=16m).

To check further the validity of the connecting boundary condition, a solitary wave propagating with an angle of incidence of 40 degree is investigated. In figure 4.6 a sequence of snapshots of free-surface displacement is shown. As we can see in figure 4.6 the connecting boundary condition works well in case when information comes from the inclined direction. Figure 4.7 shows the free surface profile along the diagonal line (from γ to δ in Figure 4.2). The results are similar to the normal incidence case. The nested grid model results in the region B and C lie between uniform grid model of high resolution and low resolution. These results provide strong evidence that the connecting boundary condition can handle well when the incoming wave is propagating in an oblique angle to the connecting boundary.

REGION A

REGION B

REGION C

Point c

Point b

Point a

x (gird No.)

β

δ

γ

α

x / h

50

40

30

20

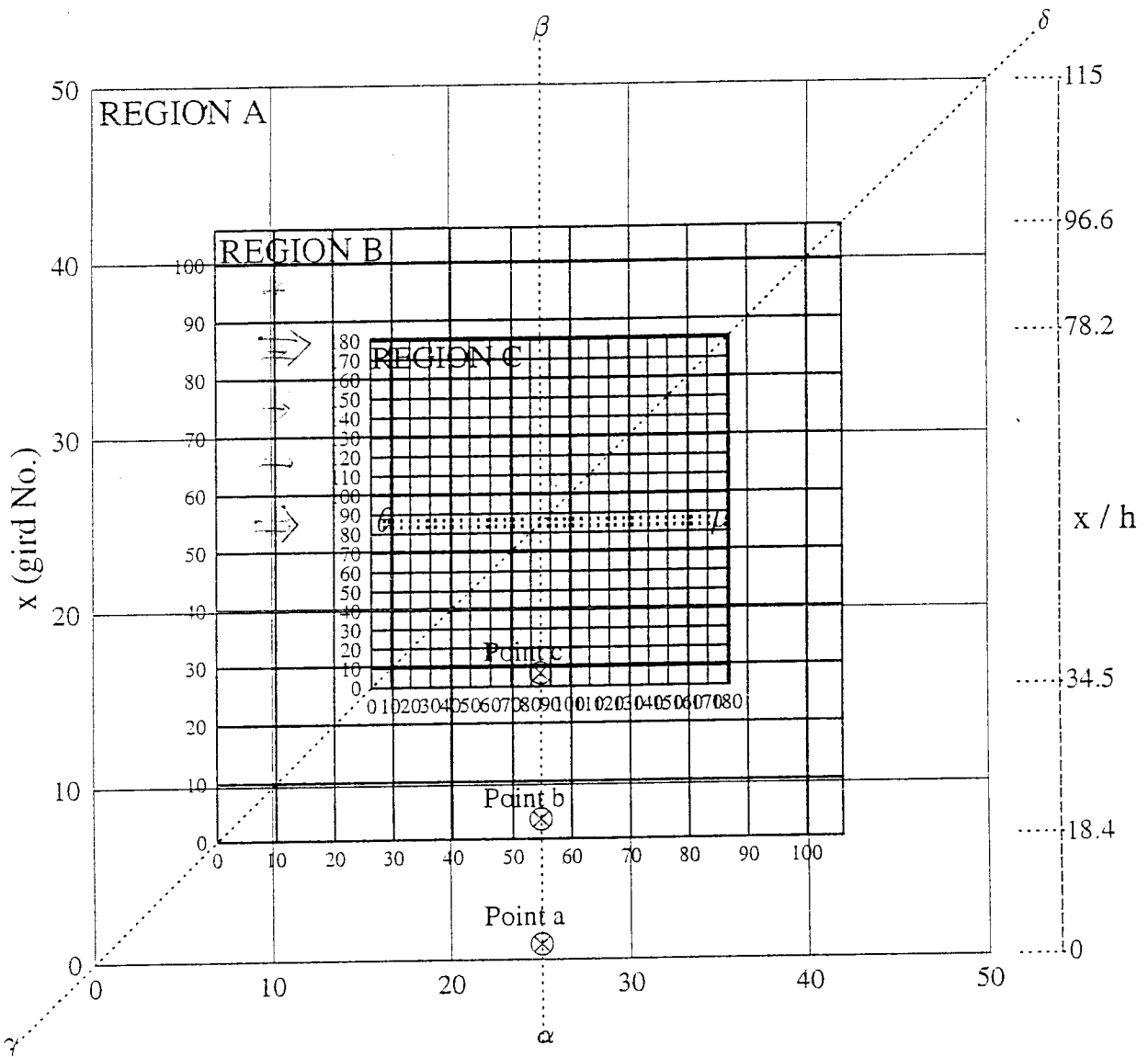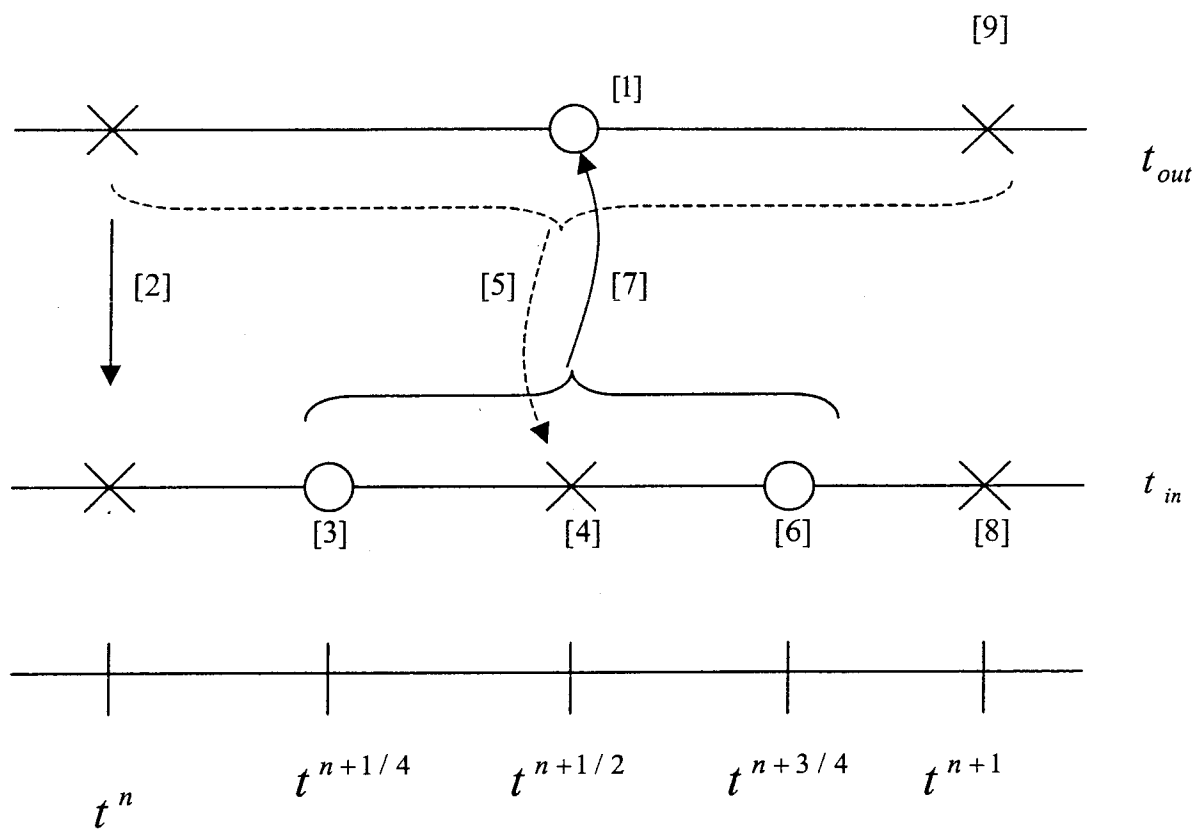10

0

0   10   20   30   40   50

115

96.6

78.2

34.5

18.4

0

Figure 4.2: A Computational Domain for Multi-grid Coupled model

31

[9]

[1]

t_{out}

[2]
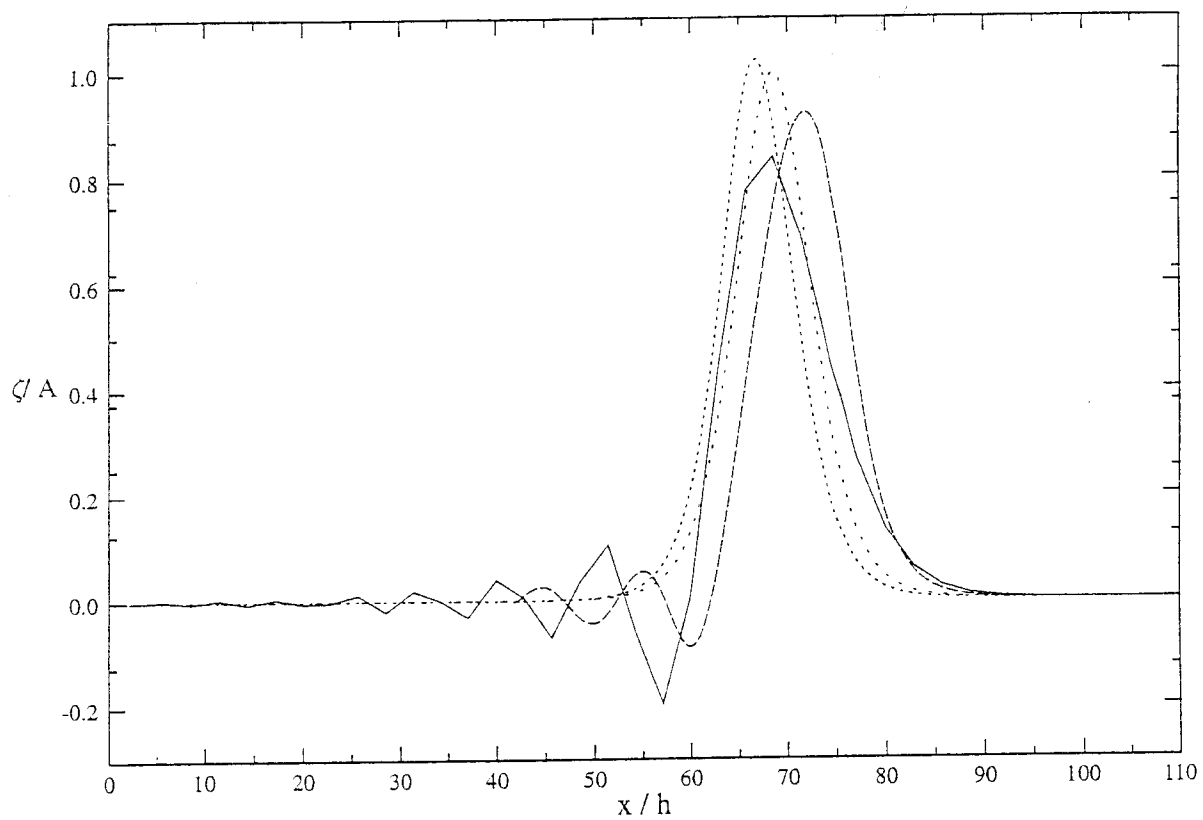
[5] [7]

[3] [4] [6] [8]

t_{in}

$t^{n+1/4}$ $t^{n+1/2}$ $t^{n+3/4}$ t^{n+1}

t^n
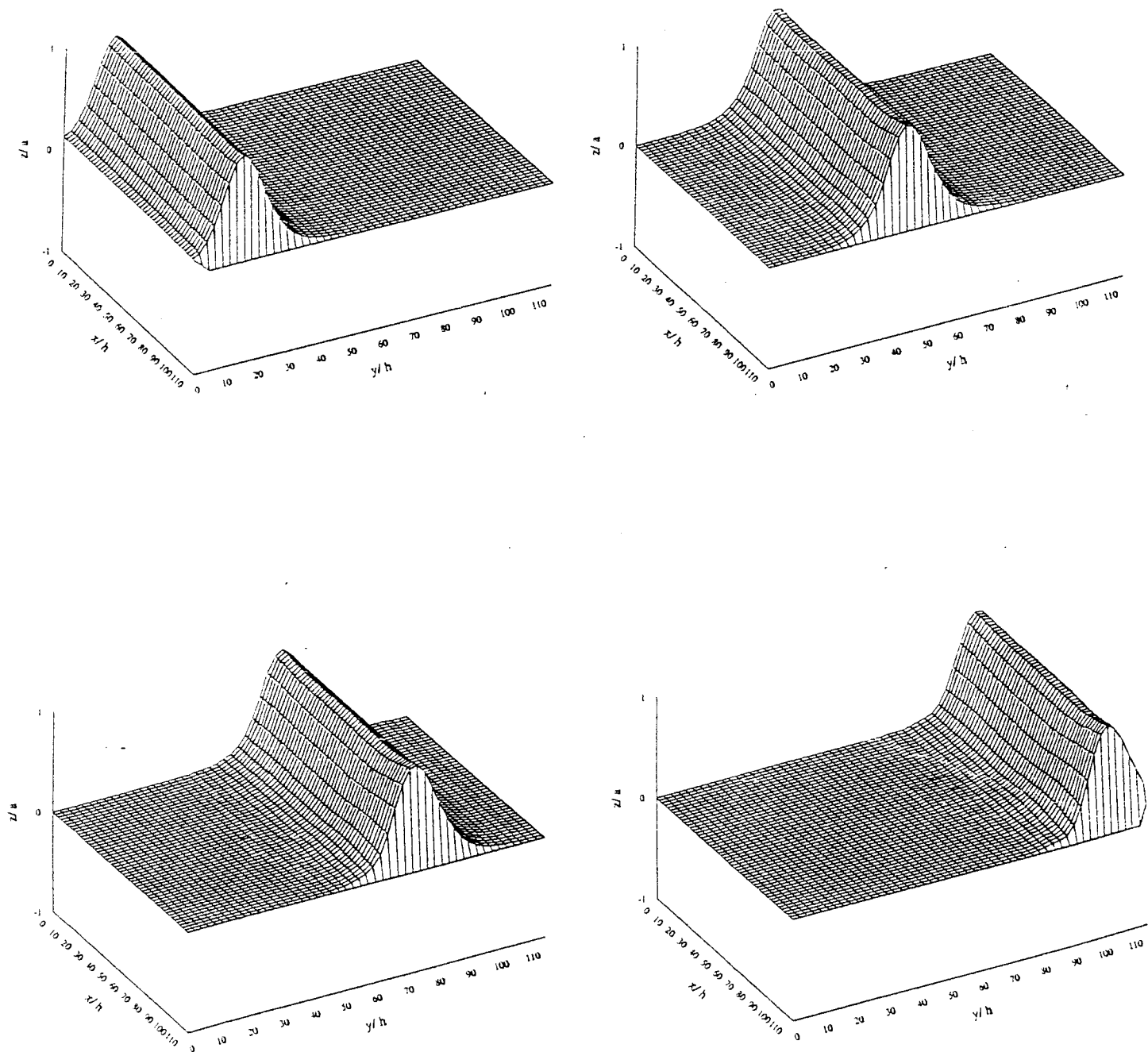
Figure 4.3: Propagation of Solitary Wave (Normal Incidence)
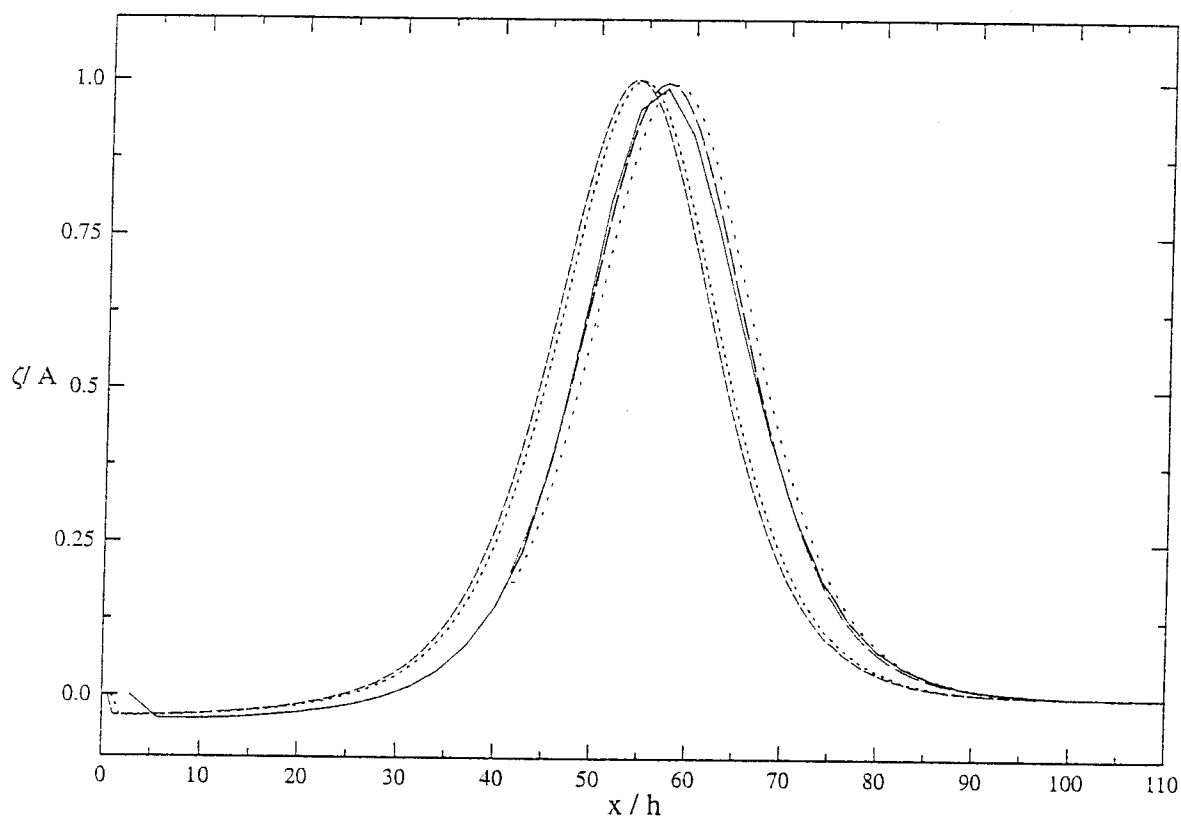
nonlinearity (A / h) = 0.01, h = 30 m, A = 0.3m

——— Not coupled (dx = 81m)
······ Not coupled (dx = 27m)
––––· Not coupled (dx = 16m)
· · · · Coupled (1:3 twice, dx = 81m : 27m : 9m
–– –– Coupled (1:5 twice, dx = 81m : 16m : 3.2m)

Figure 4.4: Water Surface Distribution along the Central Line (Normal Incidence)

nonlinearity (A / h) = 0.05, h = 30 m, a = 1.5 m

—— Not coupled (dx = 81m), t=3 min
······ Not coupled (dx = 16m)
— — Coupled (1:3 twice, dx = 81m : 27m : 9m
· · · · Analytic Solution

Figure 4.5: Water Surface Distribution along the Central Line (Normal Incidence)
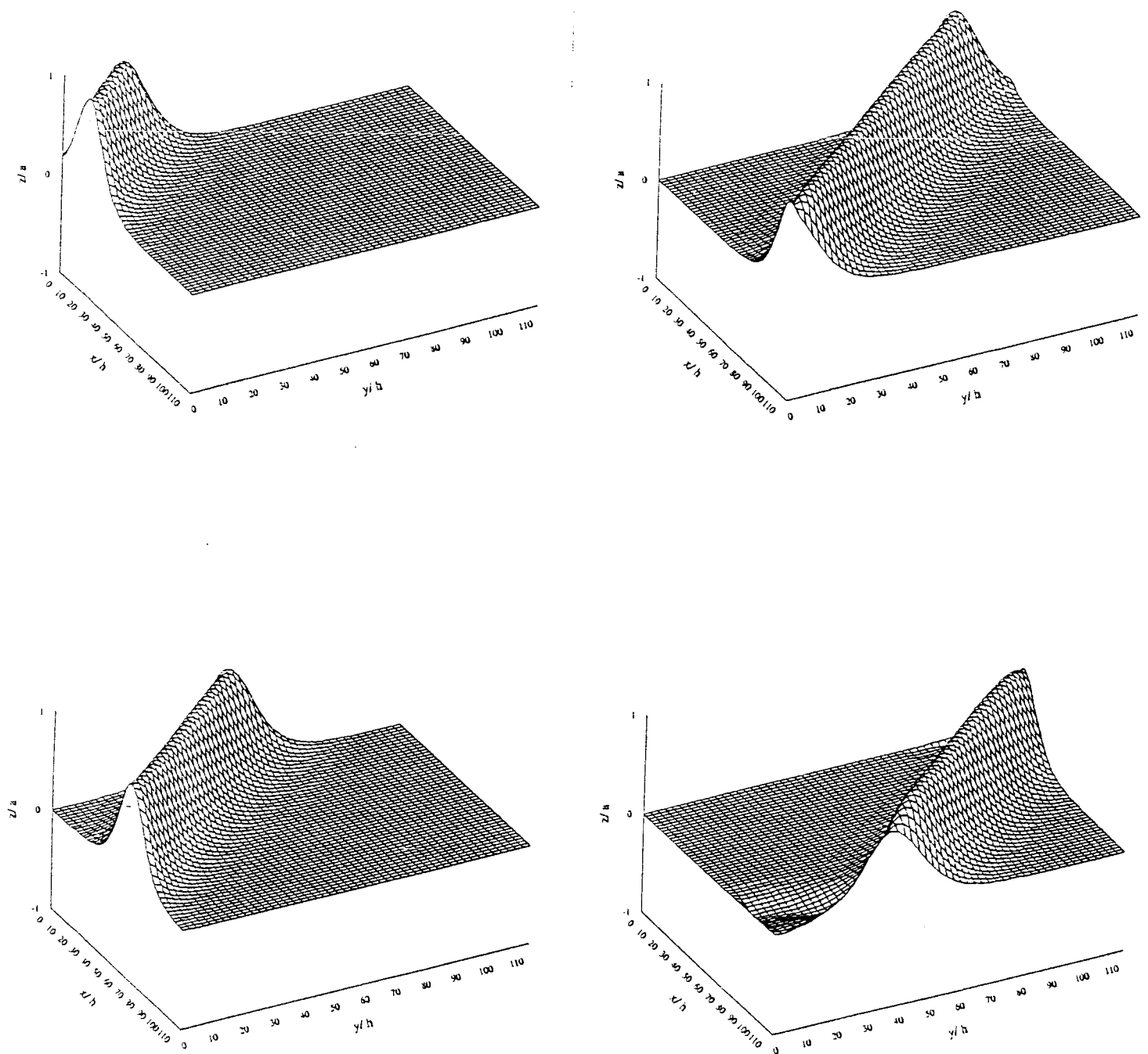
Figure 4.6: Propagation of Solitary Wave (Oblique Incidence)
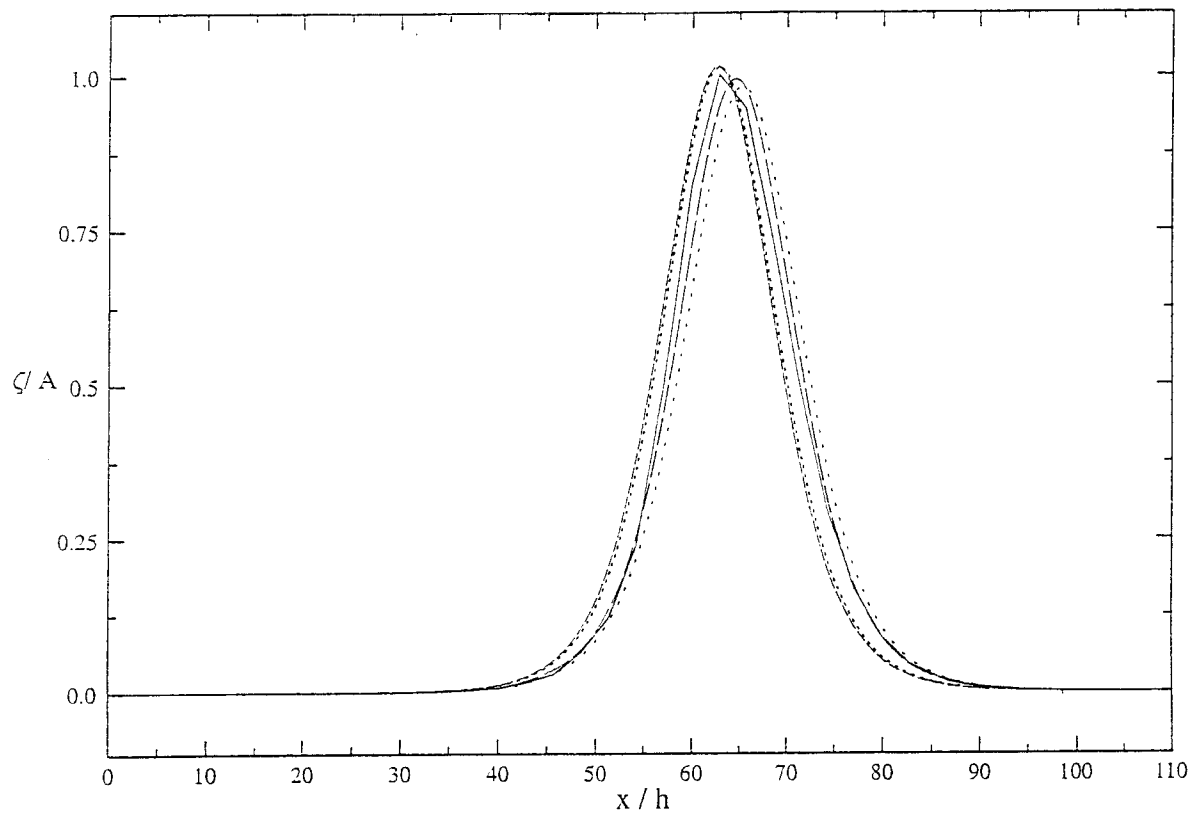
nonlinearity (A / h) = 0.01, h = 30 m, A = 0.3m

——— Not coupled (dx = 81m)
······ Not coupled (dx = 27m)
– – – Not coupled (dx = 16m)
· · · · Coupled (1:3 twice, dx = 81m : 27m : 9m)
— — Coupled (1:5 twice, dx = 81m : 16m : 3.2m)

Figure 4.7: Water Surface Distribution along the Central Line (Oblique Incidence)

36

4.3.2 Reflection of Solitary Wave

Up to now, we have investigated the suitability of the the connecting boundary condition for a solitary wave propagation. For a more complex wave propagation problem, the boundary condition needs to handle the situation where the incoming wave and outgoing wave coexist across the connecting boundary. A simple example is the intersection between incident and reflected wave in front of a solid object. To simulate this case two solitary wave is sent at the boundary in such a way that the second solitary wave can meet the refleced first solitary wave at the connecting boundary. We made a very thin vertical wall in the middle of region C in figure 4.2. (from θ to μ) A sequence of snapshots of free-surface displacement when the vertical wall exist is shown in figure 4.8. Generally speaking, the nested grid model describes the reflected wave well. We cannot see any extraordinary phenomena when reflected wave passing three different region. Since no analytical solution is available in this case, we compare the numerical solutions of the nested grid model with those of high resolution uniform grid model to verify the connecting boundary condition.

A sequence of snapshots of free-surface displacement along the center in the domain is shown in figure 4.9. At $t = 3$ (min), the second solitary wave is coming from the left boundary and at that time the first solitary wave is reflected at the vertical wall. And these two waves are intesect each other at $t = 4$ min at the connecting boundary. The nested model overestimate the free surface elevation at the connected boundary but overall transmission of two waves is generally well represented as we can see in the figure at $t = 5$ (min). The overestimation tells us that the connecting boundary scheme might be inaccuate when nonlinear interaction is strong.

Figure 4.10 shows a time history of free-surface displacements at the point a,b and c, calculated from the nested-grid model and the uniform grid model. Note that these points are selected very close to the connecting boundary. We can see a a slight

difference especially at point c which locate very near the vertical wall. The peak interaction can be detected at $t = 4$ (min) in plot (b). As we can see there is some phase shift but the maginutede of maximum amplitude is almost similar.

Until now, our test have been performed on the constant water depth. In our second example we would like to test the nested-grid model if it could represent the reflective wave which occurs when the long wave propagates from shallow water depth to deep water depth. The water depth is abruptly changed into very deep at the middle of the computational domain. In figure 4.11 a sequence of snapshots of free-surface displacement is shown. Since the advective term is considered in the region C, the general feature of propagation in the middle region shows a little bit different from that of outer region. However no additional numerical error is observed.

As previous case, the numerical solution of the nested-grid model is compared with that of the uniform grid high resolution model. Time history of free-surface displacement at the point a,b and c is shown in figure 4.12 and the comparison is made. The result is very similar to that of the previous case. In other words, this model can also represent the reflected wave due to the abrupt change of water depth within the same range of numerical errors as the case where wave is reflected by vertical wall. Due to this possibility we could expected that this model can represent the wave which is trapped in the shelf region.
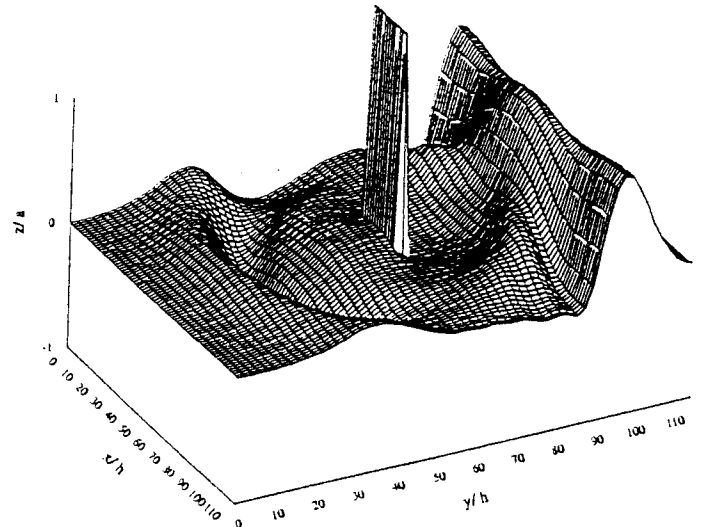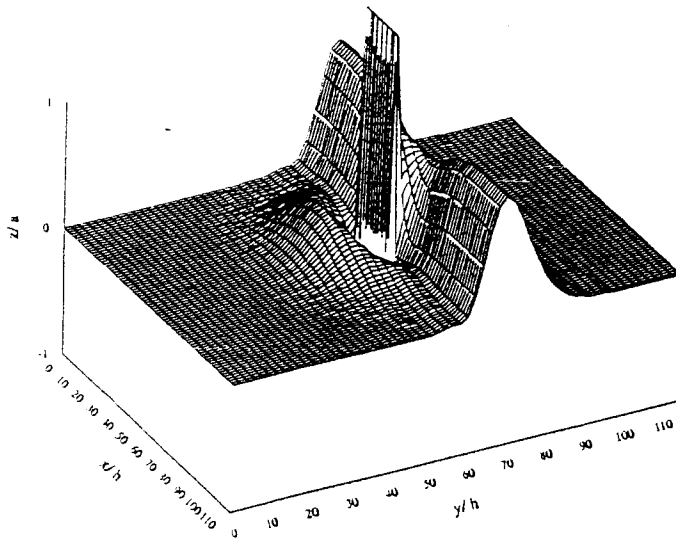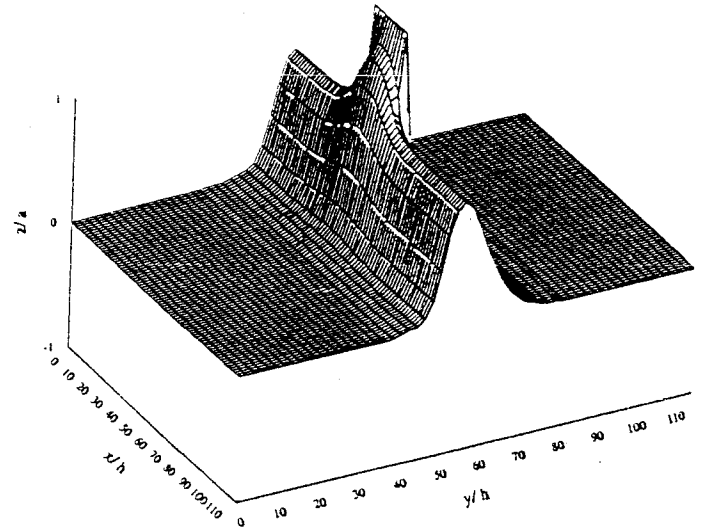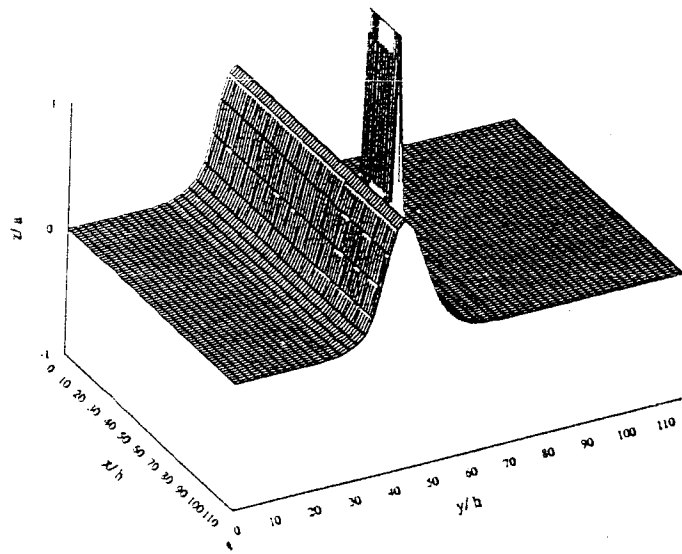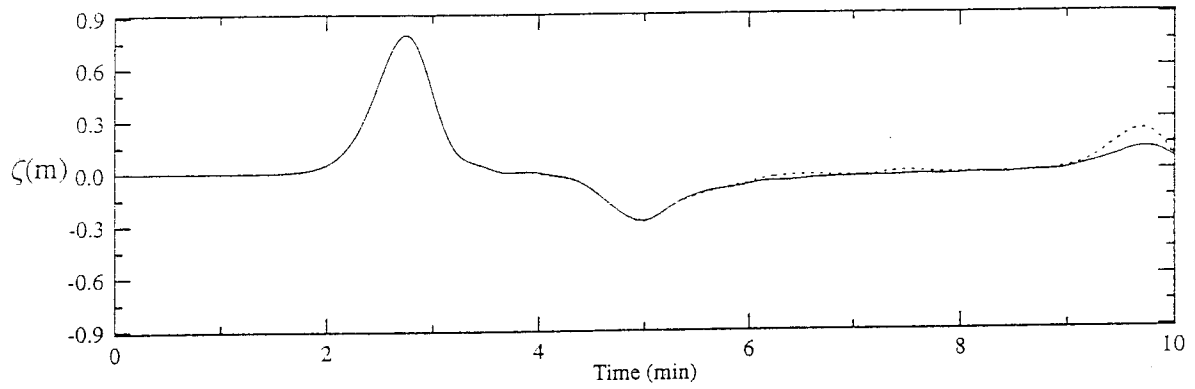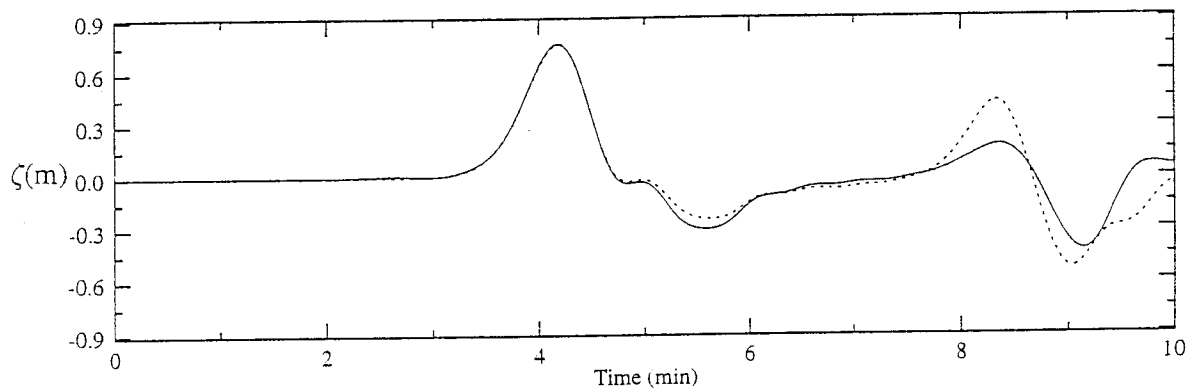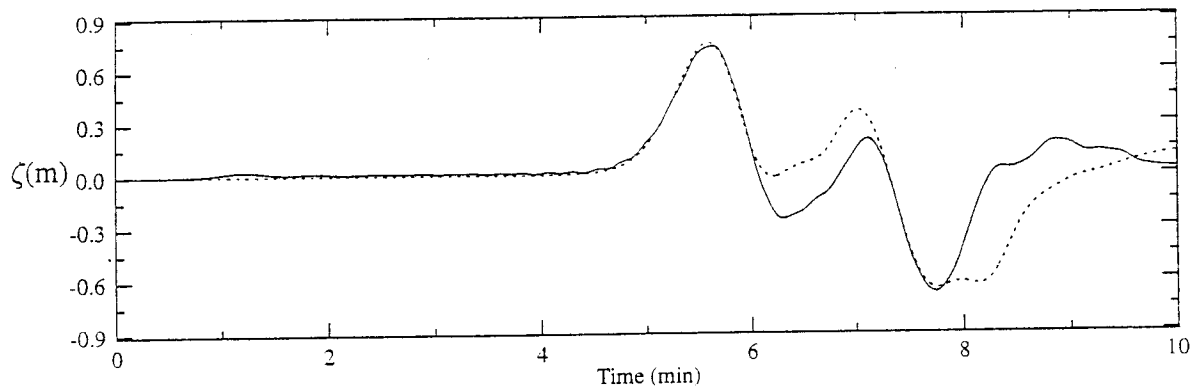
Figure 4.3: Solitary Wave Propagation and Reflection through Vertical Wall

(a) x = 6

(b) x = 16

(c) x = 26

——— Not coupled
········· Coupled, region B Nonlinear

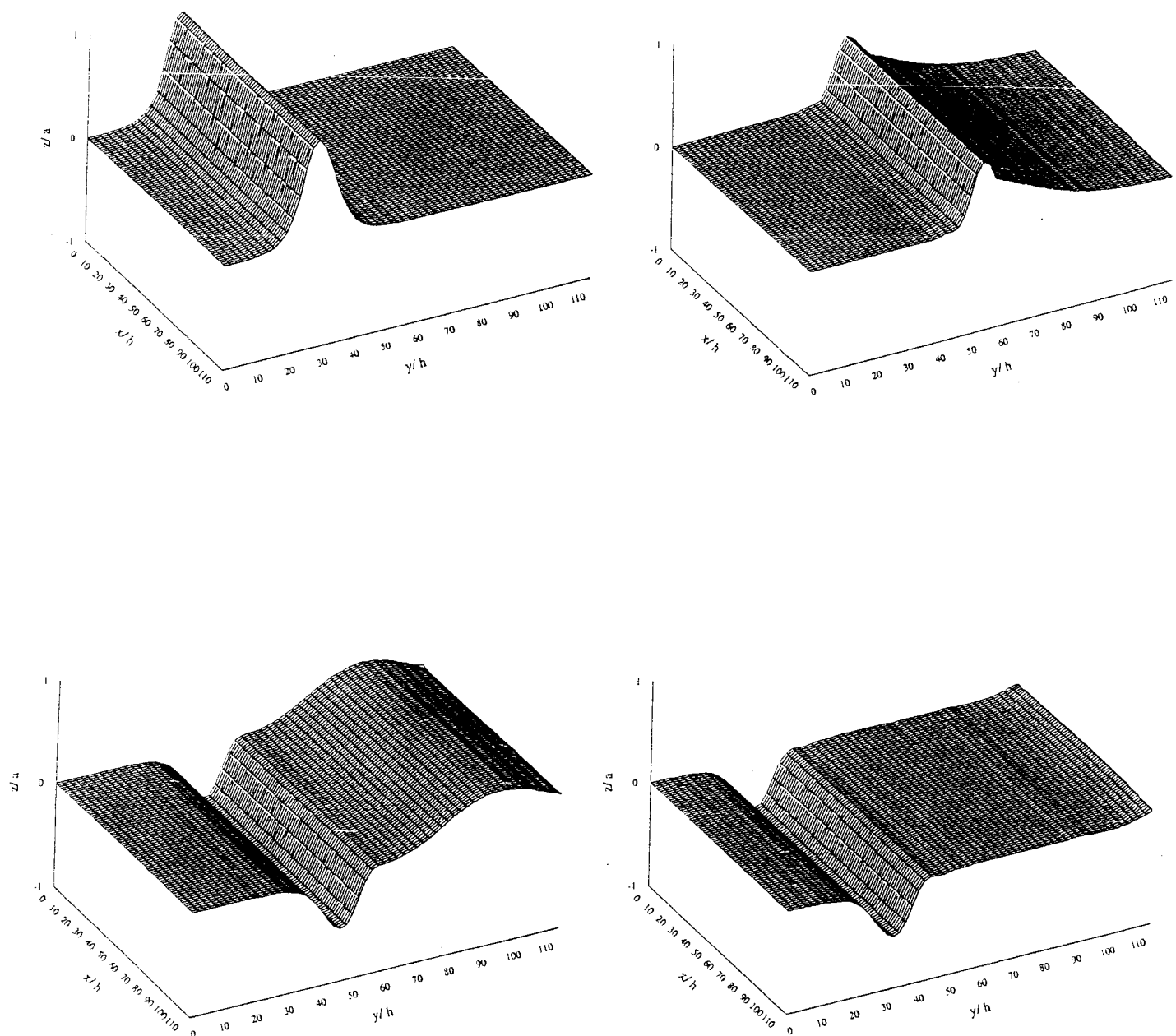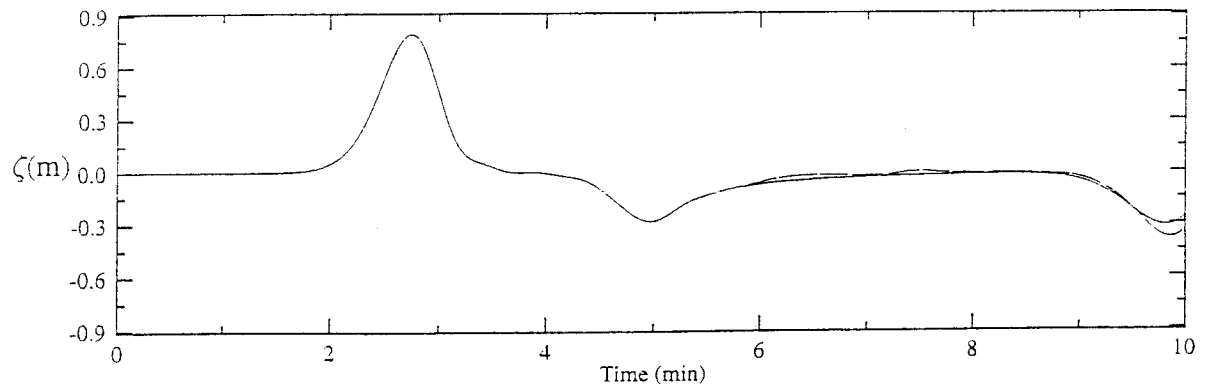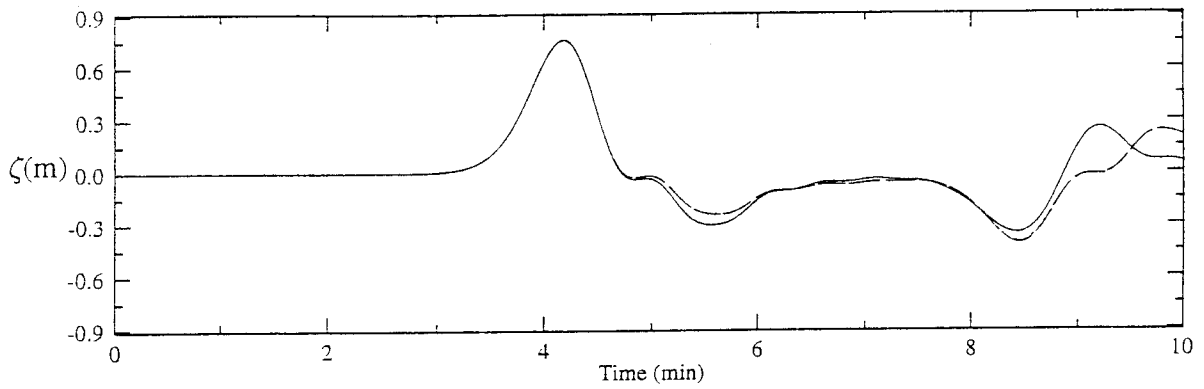Figure 4.9: Time History of Water Surface Elevation at point X= 6,16,26

Figure 4.10: Solitary Wave Propagation and reflection through Abrupt Change of Depth

(a) x = 6

(b) x = 16

(c) x = 26

——— Not coupled
— — Coupled, region B Linear
· · · · · Coupled, region B Nonlinear

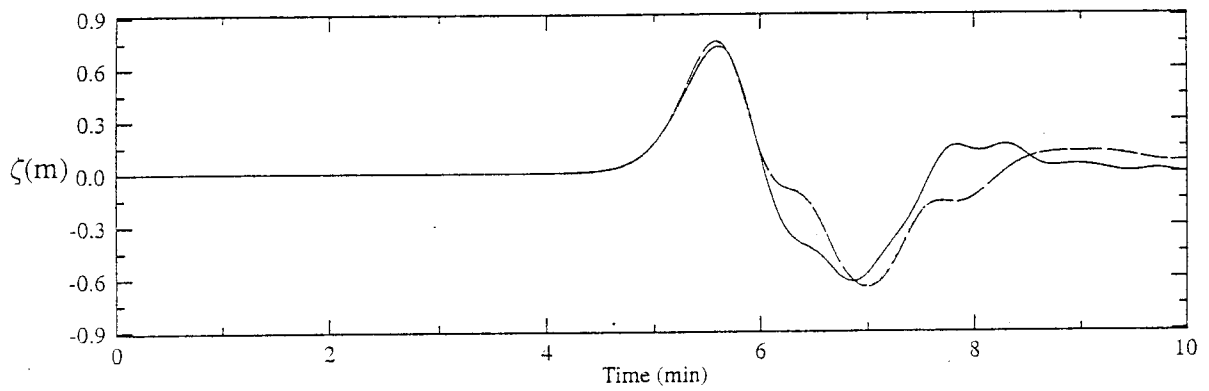Figure 4.11: Time History of Water Surface Elevation at point X= 6,16,26

5   Case Study - 1986 Hwa-Lien (Taiwan) Tsunami

Taiwan is located in a young and active Circum-Pacific Ocean Belt on the boundary between the Eurasian and Philippine Sea plates. Historically, Taiwan has suffered from several damaging tsunamis. Fortunately, in recent years it has been relatively uneventful. The most recent recorded local tsunami occurred on November 14, 1986, which was generated by an earthquake whose epicenter was about 60 km offshore of Hwa-Lien. Tide gage data inside the Hwa-Lien harbor as well as those at Ishigaki island and Miyako-Jima island indicated that a small tsunami was generated.

In this section, numerical models described in previous sections are applied to the 1986 Hwa-Lien (Taiwan) tsunami. Using the available tide gage data, the source region parameters are evaluated. Through this exercise, we would also like to achieve better understanding of the dynamic interaction between harbor oscillations and trapped waves on the continental shelf.

This earthquake occurred very close to the coastline of east side of Taiwan. It is estimated that the fault zone is about 35 km long and 35 km wide and the displacement of the fault is about 3.5 m. The orientation of the fault is N33°E. The focal depth of the slip is estimated at 13.9 km with a 50° slip angle and a 30° dip angle (Kanamori and Ciper, 1974; Kanamori and Anderson, 1975). Using these estimated fault parameters, the initial free surface displacement can be estimated (Mansinha and Smylie, 1971). The wavelength of the initial tsunami form is roughly 60 km and the maximum wave height is about 0.8 m. The leading wave of the tsunami arrived at Hwa-Lien about 10 to 15 minutes after the earthquake.

First, the linear model with spherical coordinate is applied to the computational region which covers the whole Taiwan region including the Taiwan strait. By this simulation we could understand the general feature of 1986 Hwa-Lien tsunami, which

Table 5.1: The parameters of the 1986 Taiwanese earthquake for fault model

parameter	value
length of fault (L)	35.0 km
width of fault (W)	35.0 km
orientation of fault (θ)	N33°E
dip angle (δ)	30°
slip angle (λ)	50°
displacement of fault (U)	3.5 m
focal depth (d)	13.9 km

is similar to the case of the wave propagation around a circular island.

To investigate the effect of tsunami in the Hwa-Lien harbor, we apply the multi-grid coupled model, which mainly covers the eastern side of Taiwan. To verify our proposed initial conditions, a comparison between the recorded data and the numerical result is made in terms of arrival time and magnitude of the leading wave.

5.1 Initial Free Surface Profile

The determination of the initial free surface displacement of a tsunami from the seismological data is a very difficult and unsolved issue. The parameters used to determine the initial free surface displacement are summarized in the table 4.1. The detailed description of the theory can be found in the literature (e.g., Mansinha and Smylie, 1971).

The computer program contains an algorithm determining the initial free surface profile. We here briefly describe the procedure of the estimation of initial free surface profile of tsunami proposed by Mansinha and Smylie (1971). According to Mansinha and Smylie, the initial free surface profile is consisted of two components, that is the strike-slip displacement and the dip-slip displacement. A coordinate system ξ measured positive down the fault dip as plotted in figure 5.1 is introduced for simplicity.

The analytical expression of the strike-slip displacement is given by

$$u_i = \mu U_1 \int_d^D \int_{-L}^L \left[\left(\frac{\partial u_i^1}{\partial \xi_2} + \frac{\partial u_i^2}{\partial \xi_1} \right) \sin \delta - \left(\frac{\partial u_i^1}{\partial \xi_3} + \frac{\partial u_i^3}{\partial \xi_1} \right) \cos \delta \right] d\xi_1 d\xi \qquad (5.1)$$

The analytical expression of the dip-slip displacement is given by

$$u_i = \mu U \int_d^D \int_{-L}^L \left[2 \left(\sin \delta \frac{\partial u_i^2}{\partial \xi} - \cos \delta \frac{\partial u_i^3}{\partial \xi} \right) + \left(\frac{\partial u_i^3}{\partial \xi_2} - \frac{\partial u_i^2}{\partial \xi_3} \right) \right] d\xi_1 d\xi \qquad (5.2)$$

in which the rectangular fault surface is assumed to extend over the ranges of $-L \leq \xi_1 \leq L$ and $d \leq \xi \leq D$ as shown in figure 5.1.

After some algebra we finally derive the following expressions for the integrals of the strike-slip displacement as:

$$\frac{12\pi}{U_1} u_1 = (x_1 - \xi_1) \left[\frac{2 \, r_2}{R \exp(a_1)} - \frac{4 \, q_2 - 2 \, x_3 \cos \delta}{S \exp(a_2)} \right]$$

$U_g^1 = U \cdot \cos \lambda$

$U_d = U \cdot \sin \lambda$

$$- (x_1 - \xi_1) \left[\frac{3 \tan \delta}{\exp(a_4)} - \frac{b_{10}}{S^3} + \frac{b_{12}}{q_2 \, \cos \delta} \frac{b_{13}}{b_{14}} \right]$$

$$- 6 \tan^2 \delta \, \tan^{-1} \left[\frac{(k - q_2 \cos \delta)(S - k) + (q_3 + \xi) \, k \, \sin \delta}{(x_1 - \xi_1)(q_3 + \xi) \, \cos \delta} \right]$$

$$+ 3 \tan^{-1} \left[\frac{(x_1 - \xi_1)(r_3 - \xi)}{r_2 \, R} \right] - 3 \tan^{-1} \left[\frac{(x_1 - \xi_1)(q_3 + \xi)}{q_2 \, S} \right] \qquad (5.3)$$

$$\frac{12\pi}{U_1} u_2 = \sin \delta \, (b_2 \, a_4 - a_1 - b_1 \, a_2) + \frac{b_3 \, r_2}{R \exp(a_1)} + \frac{b_5}{r_2 R}$$

$$- 2 \sin \delta \, \frac{2 x_3 (q_2 \cos \delta - q_3 \sin \delta) + q_2 \, b_4}{b_9} - 3 \tan \delta \, \frac{x_2 - \xi_2}{\exp(a_4)}$$

$$+ 2 \, \frac{q_2 \cos \delta - q_3 \sin \delta - x_3 \sin^2 \delta}{S} + b_{10} \, \frac{x_2 - \xi_2 + q_3 \cos \delta}{S^3} - b_{12} \, \tan \delta \, \frac{b_{13}}{b_{14}} \qquad (5.4)$$

$$\frac{12\pi}{U_1} u_3 = \cos \delta \, (a_1 + b_1 \, a_2 - b_2 \, a_4) + \frac{b_3}{R} + 2 \, \sin \delta \, \frac{b_4}{S}$$

$\zeta \Longleftrightarrow j$

$$- \frac{b_5}{R \exp(a_1)} + \frac{b_7 - b_8}{S \exp(a_2)} + \frac{b_{10} \, b_{11}}{S^3} - \frac{b_{12} \, b_{13}}{b_{14}} \qquad (5.5)$$

47

The final expressions of the dip-slip displacement are given as:

$$\frac{12\pi}{U} u_1 = (x_2 - \xi_2)\, \sin\delta \left[\frac{2}{R} + \frac{4}{S} - \frac{4\,\xi_3\,x_3}{S^3} - \frac{3}{\exp(a_4)} \right]$$

$$- \cos\delta \left[3\,a_4 + 2\,(x_3 - \xi_3) \left(\frac{1}{R} + \frac{2}{S} \right) + \frac{4\,\xi_3\,x_3\,(x_3 + \xi_3)}{S^3} \right]$$

$$+ 3\,\sec\delta\,(a_4 - \sin\delta\,a_2) + 6 x_3 \left[\frac{\cos\delta}{S} - \frac{q_2\,\sin\delta}{b_9} \right] \qquad (5.6)$$

$$\frac{12\pi}{U} u_2 = \sin\delta \left[-a_5 + a_6 + \frac{4\xi_3\,x_3}{S \exp(a_6)} + \frac{3(x_1 - \xi_1)}{\exp(a_4)} \right]$$

$$+ \sin\delta(x_2 - \xi_2)^2 \left[\frac{2}{R \exp(a_5)} + \frac{4}{S \exp(a_6)} - 4\,\xi_3\,x_3\,\frac{S + \exp(a_6)}{S^3\,(\exp(a_6))^2} \right]$$

$$- \cos\delta\,(x_2 - \xi_2) \left[\frac{2\,(x_3 - \xi_3)}{R \exp(a_5)} + \frac{4\,(x_3 - \xi_3)}{S \exp(a_6)} + 4\,\xi_3\,x_3\,(x_3 + \xi_3)\,\frac{S + \exp(a_6)}{S^3(\exp(a_6))^2} \right]$$

$$- 3\cos\delta \left[2\tan^{-1} \left[\frac{(x_1 - \xi_1)\,(x_2 - \xi_2)}{(h + x_3 + \xi_3)(S + h)} \right] - \tan^{-1} \left[\frac{(x_1 - \xi_1)\,(r_3 - \xi)}{r_2 R} \right] \right]$$

$$- 6\cos\delta\,\tan^{-1}\frac{(x_1 - \xi_1)(q_3 + \xi)}{q_2 S}$$

$$+ 6\sec\delta\,\tan^{-1} \left[\frac{(k - q_2 \cos\delta)\,(S - k) + (q_3 + \xi)\,k\,\sin\delta}{(x_1 - \xi_1)\,(q_3 + \xi)\,\cos\delta} \right]$$

$$+ 6 x_3 \left[\frac{-\cos 2\delta\,(q_3 + \xi) + q_2 \sin 2\delta)}{S \exp(a_6)} + \frac{(x_1 - \xi_1)\sin^2\delta}{S \exp(a_2)} \right] \qquad (5.7)$$

$$\frac{12\pi}{U} u_3 = \sin\delta\,(x_2 - \xi_2) \left[\frac{2(x_3 - \xi_3)}{R \exp(a_5)} + \frac{4(x_3 - \xi_3)}{S \exp(a_6)} - 4\,\xi_3 x_3(x_3 + \xi_3)\,\frac{S + \exp(a_6)}{S^3(\exp(a_6))^2} \right]$$

$$- 3\sin\delta \left[2\tan^{-1} \left[\frac{(x_1 - \xi_1)\,(x_2 - \xi_2)}{(h + x_3 + \xi_3)\,(S + h)} \right] - \tan^{-1} \left[\frac{(x_1 - \xi_1)\,(r_3 - \xi)}{r_2 R} \right] \right]$$

$$- 6\sin\delta\,\tan^{-1} \left[\frac{(x_1 - \xi_1)\,(q_3 + \xi)}{q_2\,S} \right] + \cos\delta \left[a_5 - a_6 - \frac{2\,(x_3 - \xi_3)^2}{R \exp(a_5)} \right]$$

$$- 4\,\cos\delta \left[\frac{(x_3^2 + x_3\,\xi_3 + \xi_3^2)}{S \exp(a_6)} + \xi_3\,x_3\,(x_3 + \xi_3)^2\,\frac{S + \exp(a_6)}{S^3\,(\exp(a_6))^2} \right]$$

$$+ 3\,x_3 \sin 2\delta \left[\frac{2\,(q_3 + \xi)}{S \exp(a_6)} + \frac{x_1 - \xi_1}{S \exp(a_2)} + \frac{q_2\,\cos 2\delta}{S \exp(a_6)} \right] \qquad (5.8)$$

$$S = \left[(x_1 - \xi_1)^2 + (x_2 - \xi_2)^2 + (x_3 + \xi_3)^2\right]^{1/2}$$
$$R = \left[(x_1 - \xi_1)^2 + (x_2 - \xi_2)^2 + (x_3 - \xi_3)^2\right]^{1/2} \tag{5.9}$$

in which S and R are distances between the field point (x_1, x_2, x_3) and the source point (ξ_1, ξ_2, ξ_3) on the fault plane and the corresponding source point $(\xi_1, \xi_2, -\xi_3)$ on the image fault plane, respectively (see figure 5.2).

$$r_2 = x_2 \sin\delta - x_3 \cos\delta, \qquad r_3 = x_2 \cos\delta + x_3 \sin\delta$$

$$q_2 = x_2 \sin\delta + x_3 \cos\delta, \qquad q_3 = -x_2 \cos\delta + x_3 \sin\delta$$

in which r_2, r_3 and q_2, q_3 are field coordinates measured normal and down dip to to the fault plane and its image, respectively. In terms of the new variables, S and R can be rewritten as:

$$S = \left[(x_1 - \xi_1)^2 + h^2\right]^{1/2} = \left[k^2 + (q_3 + \xi)^2\right]^{1/2}$$
$$R = \left[(x_1 - \xi_1)^2 + r_2^2 + (r_3 - \xi)^2\right]^{1/2} \tag{5.10}$$

in which h is the projection of S in the $x_1 = 0$ plane and k is its projection in the plane $q_3 = 0$. $h = q_2^2 + (q_3 + \xi)^2$

$k = (x_1 - \xi_1)^2 + q_2^2$

Following notations are used in equations (5.1)-(5.8) for simplicity.

$$a_1 = \ln(R + r_3 - \xi), \quad a_2 = \ln(S + q_3 + \xi)$$

$$a_3 = \ln(R + x_3 + \xi_3), \quad a_4 = \ln(S + x_3 + \xi_3)$$

$$a_5 = \ln(R + x_1 - \xi_1), \quad a_6 = \ln(S + x_1 - \xi_1)$$

$$b_1 = 1 + 3\tan^2\delta, \quad b_2 = 3\tan\delta\sec\delta$$

$$b_3 = 2r_2 \sin\delta, \quad b_4 = q_2 + x_2 \sin\delta$$

$$b_5 \;=\; 2\,r_2^2\,\cos\delta, \quad b_6 \;=\; R \,+\, 3\,\tan^2\delta$$

$$b_7 \;=\; 4\,q_2\,x_3\,\sin^2\delta, \quad b_8 \;=\; 2\,(q_2 \,+\, x_2\,\sin\delta)(x_3 + q_3\sin\delta)$$

$$b_9 \;=\; S\,(S \,+\, q_3 \,+\, \xi), \quad b_{10} \;=\; 4\,q_2\,x_3\,\sin\delta$$

$$b_{11} \;=\; (x_3 \,+\, \xi_3) \,-\, q_3\,\sin\delta, \quad b_{12} \;=\; 4\,q_2^2\,q_3\,x_3\,\cos\delta\,\sin\delta$$

$$b_{13} \;=\; 2\,S \,+\, q_3 \,+\, \xi, \quad b_{14} \;=\; S^3\,(S \,+\, q_3 \,+\, \xi)^2$$

The initial free surface profile of the 1986 Taiwanese tsunami is plotted in figure 5.3 The peak of the initial free surface profile is about $0.8\ m$ and the wavelength is about $60\ km$.
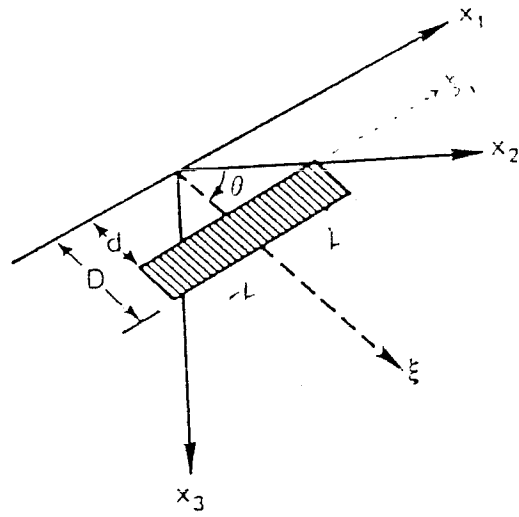
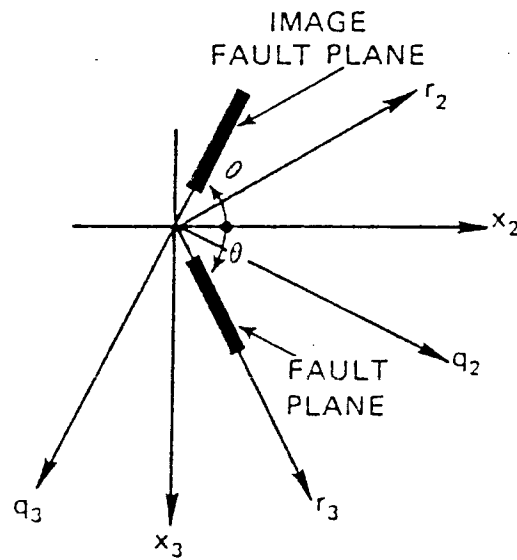Figure 5.1: The fault geometry and coordinate system

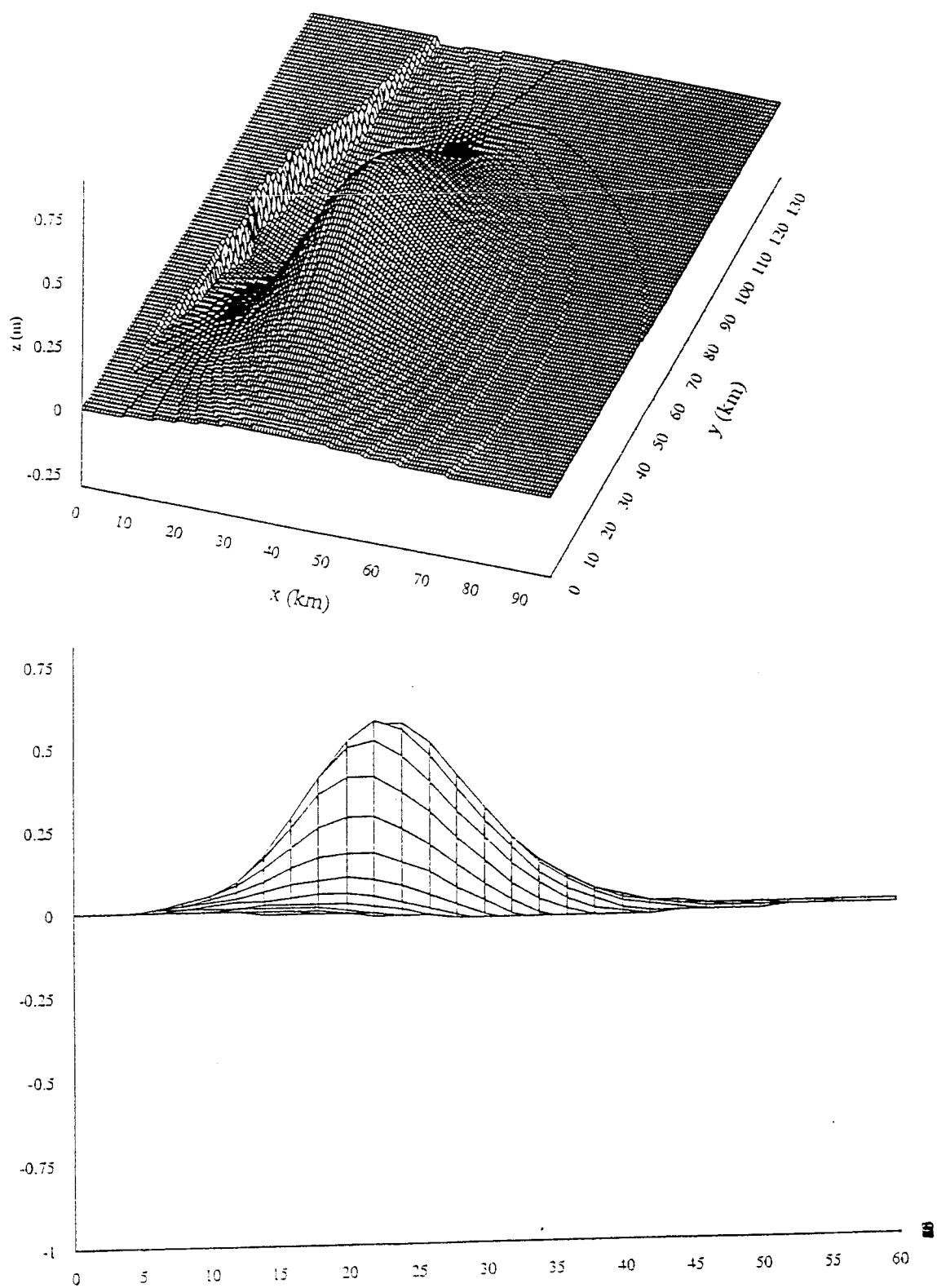Figure 5.2: The fault and image fault coordinate systems

49

Figure 5.3: The initial free surface profile

50

5.2 LINEAR Model

5.2.1 Bathymetric Data and Grid System

The bathymetric data near Taiwan is generated by digitizing the chart which is published by Taiwan. The region where the LINEAR model is applied is shown in figure 5.4 This region covers from $(118°E, 20°N)$ to $(124°E, 26°N)$ with the grid resolution of $1' \times 1'$ which is roughly $1500m \times 1830m$. The grid system in this model is 360×420 so that the area of whole computational domain is about $610km \times 770km$. To include the effect of earth curvature, a Spherical coordinate system is used in this region. As we can see in figure 5.4 the depth gradient in the eastern side of Taiwan is very steep. On the other hand the depth in western side is very shallow compared to that of eastern; less than $500 \ m$.

5.2.2 Simulation result and discussion

The distant propagation of the 1986 Hwa-Lien tsunami is calculated using the LINEAR model. The object of this simulation is to know the general feature of 1986 Hwa-Lien tsunami in large scale.

A sequence of snapshot of the contour for the propagation of tsunami is shown in figure 5.5 to 5.10 As the tsunami propagates around Taiwan, the wave front spreads over a large area, reducing the leading wave amplitude. Since the western side of Taiwan is very shallow compared with the eastern, the tsunami takes more than three hours to entirely circle Taiwan.

Figure 5.11 shows a maximum runup distribution along the eastern side of Taiwan. In this LINEAR model, the moving boundary condition is not considered, since the grid resolution is very coarse ($1.5km \times 1.8km$) and the advective term is not included. Therefore the maximum runup here means the highest water surface elevation adjacent to coastline which is regarded as a vertical wall in this model. Using

this maximum runup distribution, we can understand the concentration of the energy of tsunami. As we can see, the middle part of the eastern side seems to have most serious concentration of the 1986 tsunami where the Hwa-Lien harbor is located.